공학석사학위논문

물리적 접근법에 기반한 LQG 알고리즘 고조화 제어 시뮬레이션

Higher Harmonic Control Simulation by LQG Algorithm built on the Physics-Based Approach

2023 년 2 월

서울대학교 대학원

항공우주공학과

공 건 혁

물리적 접근법에 기반한 LQG 알고리즘 고조화 제어 시뮬레이션

Higher Harmonic Control Simulation by LQG Algorithm built on the Physics-Based Approach

지도교수 신 상 준

이 논문을 공학석사 학위논문으로 제출함

2022년 10월

서울대학교 대학원
항공우주공학과
공 건 혁

공건혁의 공학석사 학위논문을 인준함

2022년 12월

위 원 장 이 관 중

부위원장 신 상 준

위 원 김 현 진

Abstract

Higher Harmonic Control Simulation with LQG Algorithm based on the Physics-Based Approach

Kunhyuk Kong

Department of Aerospace Engineering

The Graduate School

Seoul National University

As rotorcraft experiences severe unsteady aerodynamic loads, a significant level of vibration and noise will be induced. To solve such problem, a number of methods have been attempted. Passive means such as an isolator and absorber have been examined, but those were not sufficient to meet the standard established by NASA. As a consequence, active vibration control methods have been suggested. Higher harmonic control method is one of the active control methods, and is found as the most mature and promising technique. There is a considerable amount of efforts on the higher harmonic control along with simulation. However, few of them took into account the realistic physical configuration of the rotor system.

In this thesis, higher harmonic control simulation based on the physics-based approach will be presented. The simulation configuration is based on the hardware of UH-60A Black Hawk. The rotor system consists of the blades, dampers, pitch

links, hinges, scissors, servo actuators, and a shaft. The pitch angle of the blades is controlled by the motion of the servo actuators attached to the non-rotating swashplate. The rotor system is evaluated by the comparison on the trim and modal analysis.

Next chapter, an algorithm for the present higher harmonic control algorithm will be introduced. Based on the linear quadratic Gaussian (LQG), optimal control gain for vibration reduction will be achieved. The system identification and variable reduction are achieved by MATLAB computation. Then, higher harmonic control simulation will be executed by DYMORE2, a multibody dynamics software. The vibration reduction capability is validated with the simulation results.

Finally, fuselage modeling will be discussed. To include the fuselage reaction, Herting's model order reduction approach will be introduced. By applying Herting's method, the degrees of freedom of the substructure will be reduced into those of the modal coordinate. To verify the model order reduction capability, modal and transient dynamic analyses on a rectangular hollow beam will be analyzed. Then the details of the structure to imitate the fuselage reaction will be given.

Keywords: Higher harmonic control, Active vibration control, Component mode synthesis

Student Number: 2021-20832

Contents

List of Tables

Page

List of Figures

Page

Chapter 1

Introduction

1.1 Background and Motivation

Rotorcraft experiences severe vibratory excitation induced upon both the rotor and fuselage. It also faces aeroacoustic noise emitted by the rotor because of the complex aerodynamic circumstances. Since such annoyance prevented the further utilization of the rotorcraft and VTOL for the public areas, several approaches have been attempted to alleviate the vibration. To mitigate the problem, vibration reduction methods have been examined from the standpoint of the aerodynamic and structural aspect. There have been two ways of vibration reduction – passive and active methods. Passive methods include the bifilar or pendulum absorber, isolation systems, and so on. Detailed information about the passive method is summarized in [1]. By the passive method, the vibration level of the rotorcraft has been reduced to 0.05 – 0.01g. However, it was not able to reach the level of 0.02g, which NASA council suggested as a recommended level [2]. To enforce the vibration level to become lower than the goal of 0.02g, active vibration reduction methods were investigated in parallel and higher harmonic control was one of such methods.

Higher harmonic control method is evaluated as one of the most mature methods among the active control approaches regarding the rotorcraft vibration reduction [3]. By the higher harmonic control, the pitch angles of the blades are excited by the

combination of N/rev and N±1/rev frequencies. The servo actuators attached to the nonrotating swashplate move linearly, and thus the pitch links are displaces by the motion of nonrotating and rotating swashplate. As a result, the pitch angles of the blades are perturbed by the rotation of the pitch hinges induced by the motion of the pitch links.

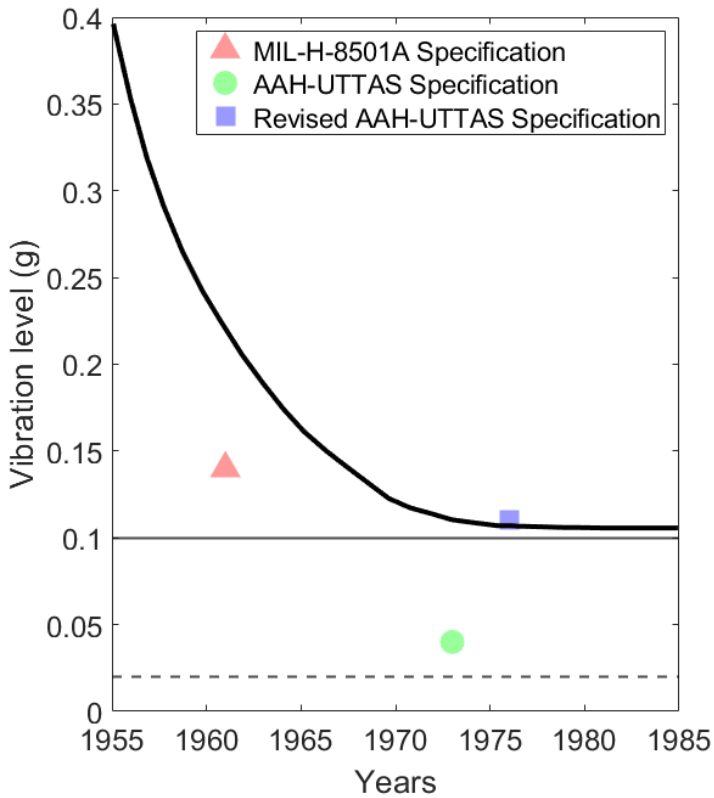

Fig. 1.1 Rotorcraft vibration level trend

Fig. 1.2 OH-6A HHC flight test instruments

Fig. 1.3 HART Ⅱ flight test instruments

1.2 Literature Review

1.2.1 Vibration reduction capability of the higher harmonic control

Throughout its long history, considerable amount of the researches has been conducted and there exist two major ways regarding the higher harmonic control methodology: ones about the advantages and disadvantages of the higher harmonic control itself, and the others about the detailed algorithms for higher harmonic control.

Research about the advantages of the higher control has focused on reduction of the hub vibratory loads and the sectional loads of the rotor blades at several stations, and the additional power requirement to implement the higher harmonic control. Plenty of analytical examinations of simulations have been attempted for it. Taylor et al. [4] achieved the results of the analytic studies on higher harmonic control for the reduction of the fuselage vibration and gust response. It was found that the reduction from 80 to 90 percent was achieved by the higher harmonic control when considering the closed-loop condition. Oleary et al. [5] executed analytical studies of the higher harmonic control on Sikorsky S-76. Since the feasibility of the higher harmonic control technique on a smaller and lighter aircraft was already obtained, their analytic study was focused on a heavier aircraft within the range from 8,000 to 10,000lbs. Results for both open- and closed-loop condition were achieved along with the result that smaller than 2° of HHC pitch angle input would be sufficient to satisfy the vibration reduction capability required.

1.2.2 Algorithm for the higher harmonic control algorithm

Researches about the algorithm for higher harmonic control focus on the advance in the speed to follow up the response of the rotor system and the enhancement of the stability and robustness of the system. Methods that have been broadly examined are T-matrix assumption approach and the continuous time controller at the specific target frequencies, i.e., N/rev and N1/rev. Johnson [6] provided an extensive summary about the higher harmonic control algorithms. There exist numerous variants of higher harmonic control algorithm, and he suggested that those algorithms share important characteristics: 1) a linear, quasi-static, frequency-domain model of rotorcrafts, 2) an identification of the plant via a Kalman filter or a least square error method, 3) a cost function in the quadratic form. In his report, the transfer matrix between the harmonic vector output z and input θ are determined. This so-called T-matrix approach has been a dominant method for higher harmonic control. Patt [7] examined an improved algorithm with the adaptive variant for higher harmonic control, and it was shown that such improved algorithm was capable of reducing the vibration effectively even when the system had been identified poorly or the nonlinearity of the system was important. The verification was performed with on-line simulation.

However, as Hall [8] suggested that most of such literatures about the algorithms for higher harmonic control were not based on the theoretical fundamental of the rotorcraft dynamics, most of approaches modeled rotorcraft by the algebraic equation.

1.3 Thesis overview

In this thesis, higher harmonic control simulation with actuators designed by the physics-based approach is proposed. The rotor system modeled for the simulation is UH-60A Black Hawk. The simulation is characterized by the summaries below:

1. The representative rotor system is suggested the hardware of UH-60 Black Hawk. The control input is the linear displacements of the servo actuators, and the output is the vibratory loads measured at the rotor shaft.

2. Unlike the precedent researches on the algorithm for higher harmonic control, which used the algorithm based on T-matrix, the algorithm used for the simulation is based on the linear quadratic Gaussian (LQG) algorithm.

3. To predict the dynamic interaction between the rotor system and the fuselage, the additional structure is attached to the rotor system. The scale of the structure is large compared to the rotor system as the scale of the fuselage is.

First, the details about the rotor system are given in Chapter 2. The components that consist of the rotor system will be listed. The verification via the comparison with the flight experiment results are executed. Modal and trim analyses are executed for the verification. The algorithm for this thesis is explained in Chapter 3. Also, the numerical results of the higher harmonic control simulation are described. The schematic of Herting's method, one of the model order reduction methods for the structural analysis, is explained in Chapter 4. The verification of the model reduction

function of DYMORE2 is executed. The function is verified via the comparison with the results of the simple modal and transient analyses by ANSYS Mechanical. Full-order model and transient analysis is completed.

Chapter 2

Rotor System Modeling

In this chapter, the present rotor system representation will be introduced. The reference rotor system is the hardware of the UH-60A Black Hawk, which is one of the most commonly used rotorcrafts among the U.S. and Republic of Korea Army. The modeling and analysis are completed by a multibody dynamics analysis software, DYMROE2. The verification of the rotor system is executed by the comparison with the flight experiment results.

2.1 Rotor system configuration

The rotor system is modeled in a similar manner to that useed by University of Munich [9]. The rotor system consists of blades, scissors, dampers, pitch links, and the shaft. The scissors have two symmetric components and both ones are rigidly connected to the shaft. The role of the scissor is to connect the rotating and non-rotating parts of the rotor system. Since UH-60A Black Hawk has the four-bladed the rotor system, there exist 4 blades on the present rotor representation. Each of the blades has the damper, hinges and pitch link attached. The dampers are modeled as the prismatic joints along with the nonlinear damping properties, and the properties are obtained based on the experiment results by NASA [10]. The dampers are attached to enhance the lead-lag stability. Also, the blades are connected to the hinges.

UH-60A Black Hawk has the articulated rotor system, so the hinges for all three direction, i.e., flapping, pitching, and lead-lag hinges are all implemented. These three hinges are modeled by revolute joints, and each of the joints represents the flapping, lead-lag, and feathering hinge. In addition, one another revolute joint is also implemented to represent the torsional spring. The pitch links are connected to the blade roots and the bottom of the pitch links are connected to the rotating swashplate part by the spherical joint. The pitch link is modeled by the uniform-section beam. The rotating swashplate parts are connected with the nonrotating swashplate parts with a revolute joint, and thus the rotation of the upper components including the rotating swashplate will be enabled. Beneath the non-rotating swashplate, the cantilever servo actuators will support the rotor system. The servo actuators have three components and are modeled by the prismatic joints. The pitch angle of the blades is controlled by the motion of the non-rotating swashplate, and the swashplate is moved by the combination of the servo actuators. The configuration of the present rotor system is shown in Fig. 2.2 and the detailed components around the shaft are illustrated in Fig. 2.3.

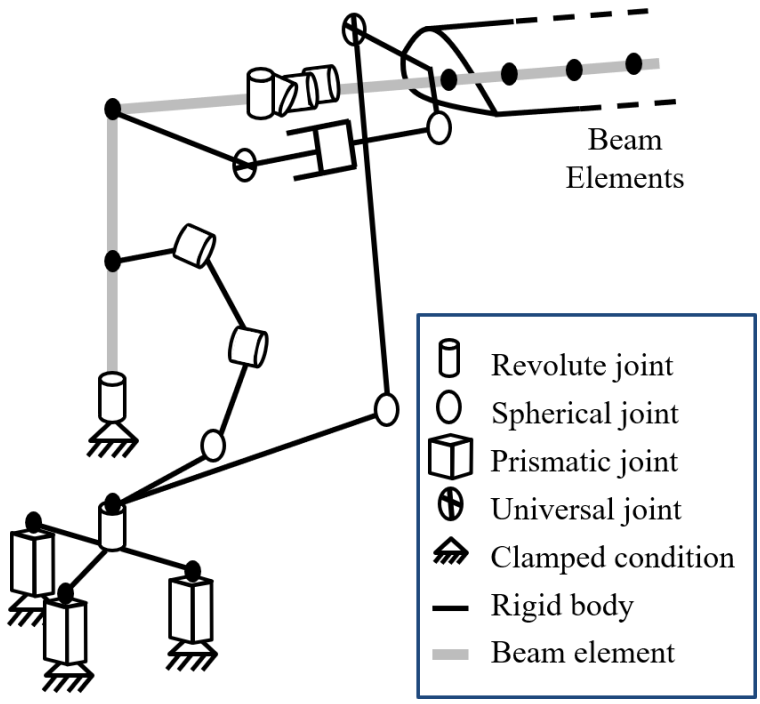

Fig. 2.1 Topology of the present rotor configuration

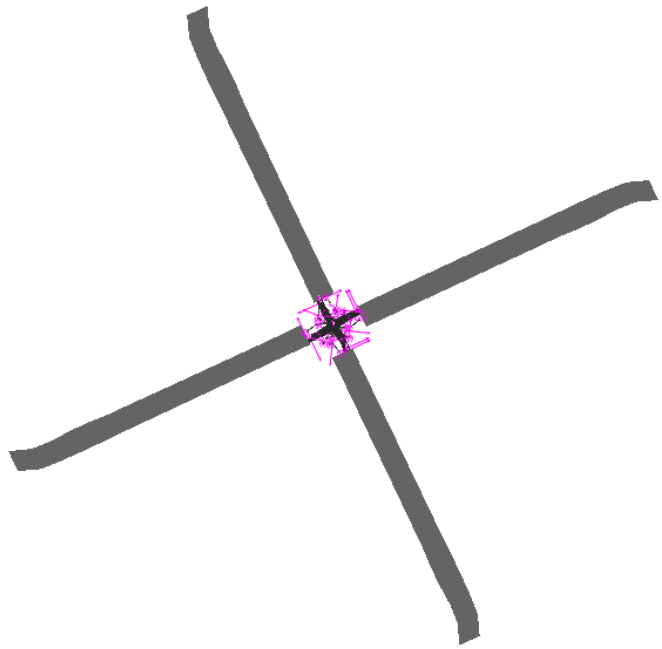

Fig. 2.2 DYMORE input representation of UH-60 rotor system

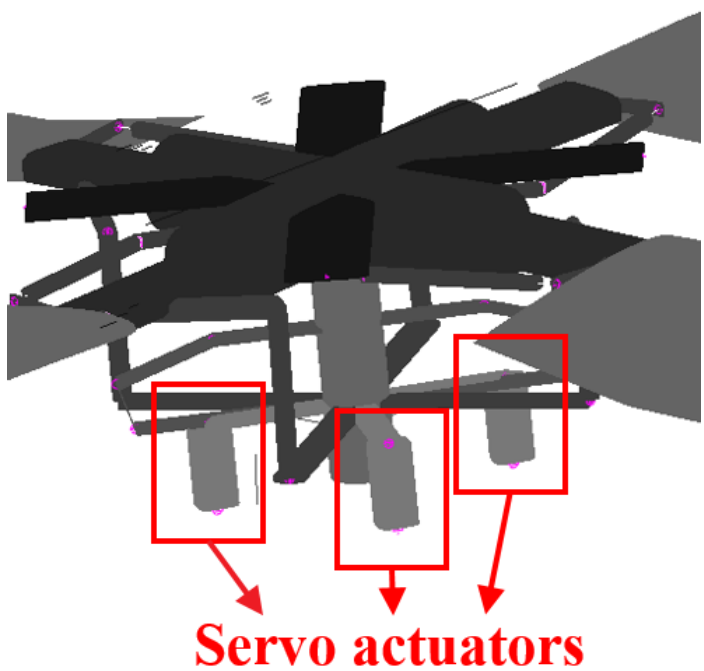

Fig. 2.3 Details of the shaft components

2.2 Rotor modeling verification

The validity of the present rotor system representation is verified by the relevant trim analysis. For such purpose, a multi-body dynamics software, DYMORE2 is used. The software is based on the geometrically exact beam and shell formulation for structural analysis. The unsteady aerodynamic analysis of the program is based on Peters-He dynamic inflow and ONERA-EDLIN dynamic stall. DYMORE2 is constructed to analyze the dynamic behaviors of the rotor system, so there is an amount of the precedent researches on rotorcrafts using DYMORE2.

Also, since the blade-vortex interaction (BVI) have an important role of the aerodynamic characteristics of rotorcraft, it is important to catch the wake behavior. For such purpose, Bhagwat-Leishman time marching free wake model [11] is additionally implemented to DYMORE2.

Structural verification is attempted first by comparison in terms of the fan plots. The reference used for the present comparison are the results by Ormiston [12], Bowen [13], Yeo [14], and Sitaraman [15]. As a result of the eigenfrequencies comparison in terms of the rotating speed of the rotor, good agreement is obtained. Both parameters are nondimensionalized. With varying stiffness of the pitch links, the lower eigenfrequencies are not affected. However, the higher eigenfrequencies, such as the first torsion, second lateral, and third flap mode frequency, are affected. Since the trim analysis that will be presented targets the results of the experiment of Yeo, the stiffness coefficient of 225,000 feet per pound is selected.

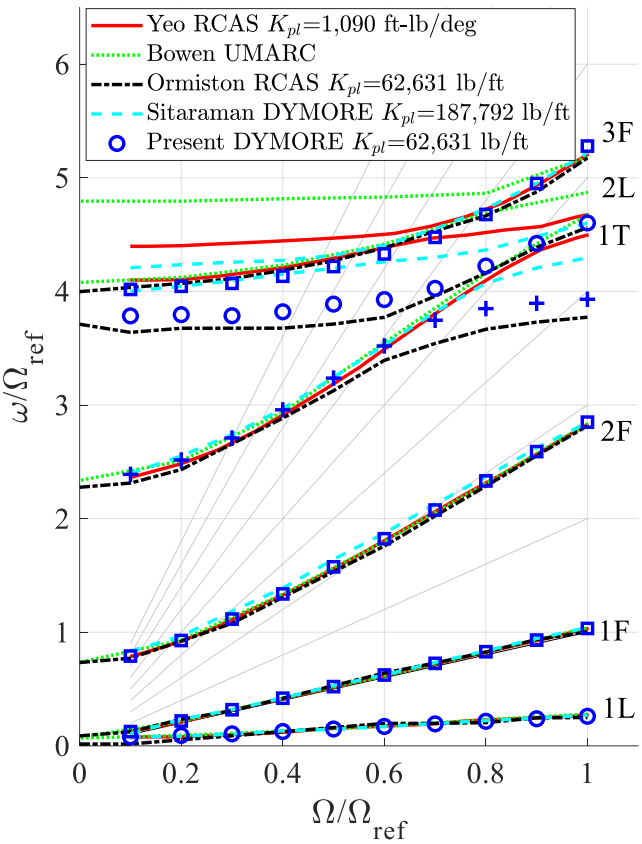

(a) fan plot of the present rotor system, $K_{pl} = 62{,}631$ lb/ft

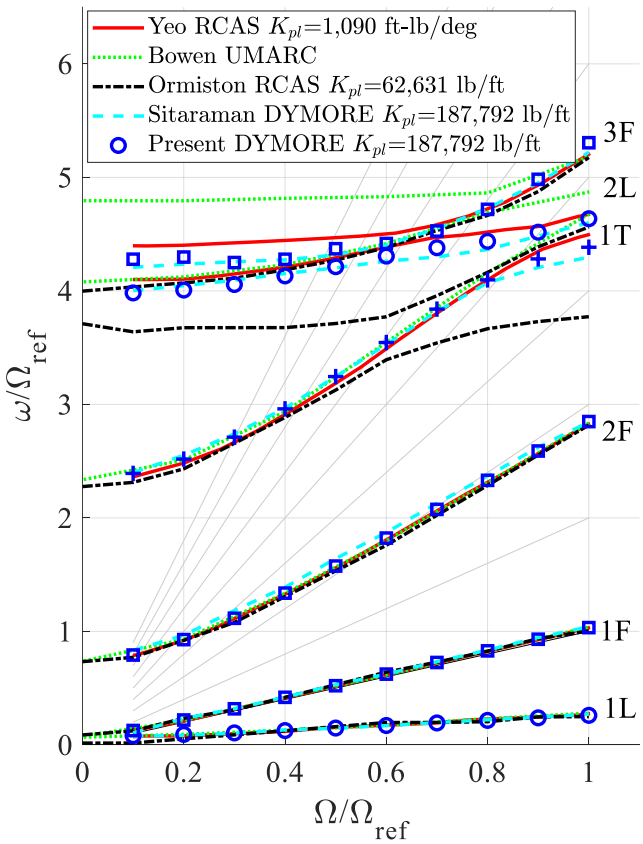

(b) fan plot of the present rotor system, $K_{pl} = 187{,}792$ lb/ft

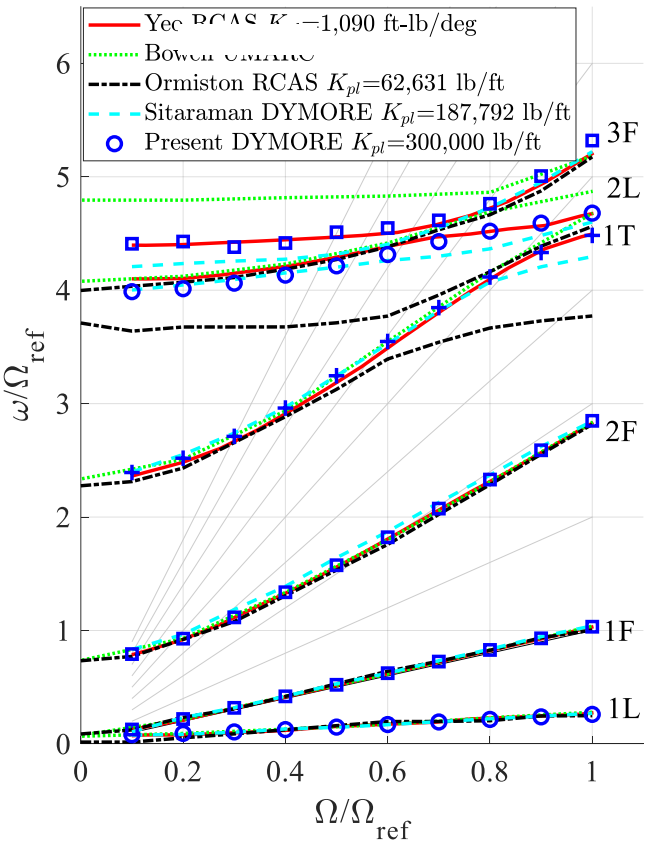

(c) fan plot of the present rotor system, $K_{pl} = 225{,}000$ lb/ft

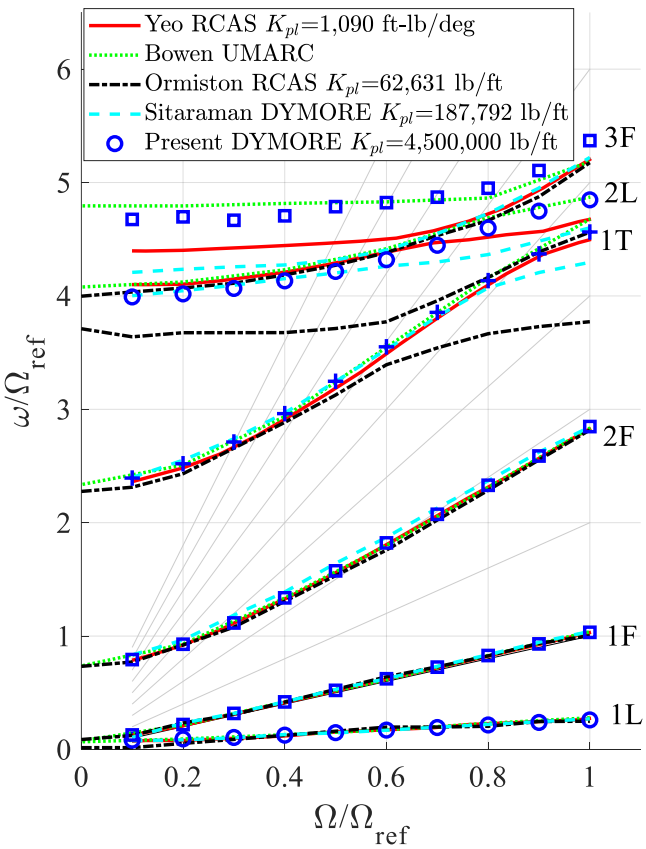

(c) fan plot of the present rotor system, $K_{pl} = 4{,}500{,}000$ lb/ft

Fig. 2.4 Fan plot in terms of the value of the stiffness coefficient in the pitch link

Also, the trim analysis for an isolated rotor is executed and the linear displacement of the servo actuators are selected as the control parameter. The present flight condition is based on the flight counter C8513, and the results for comparison are the one obtained by Yeo [13]. Flight counter 8513 is a descent maneuver condition and under that condition, blade vortex interaction (BVI) significantly affects to the rotor. The auto pilot function within DYMORE2.0 is used to adjust the displacement of the servo actuators to meet the trim parameters. The trim parameters are the amplitudes of 4/rev hub vibratory load components, i.e., the hub shear force, rolling moment, and pitching moment. The results of the present trim analysis are shown in Figs. 2.5 through 2.8. As in Fig 2.5, the auto pilot provides an initial perturbation to each displacement of the servo actuator, and the perturbation also occurs at the rotor hub loads. Via the relationship between the perturbation and the response, the auto pilot function determines an optimal displacement of the rotor hub loads. Figure. 2.6 shows the schematic of the free wake induced by the rotor.

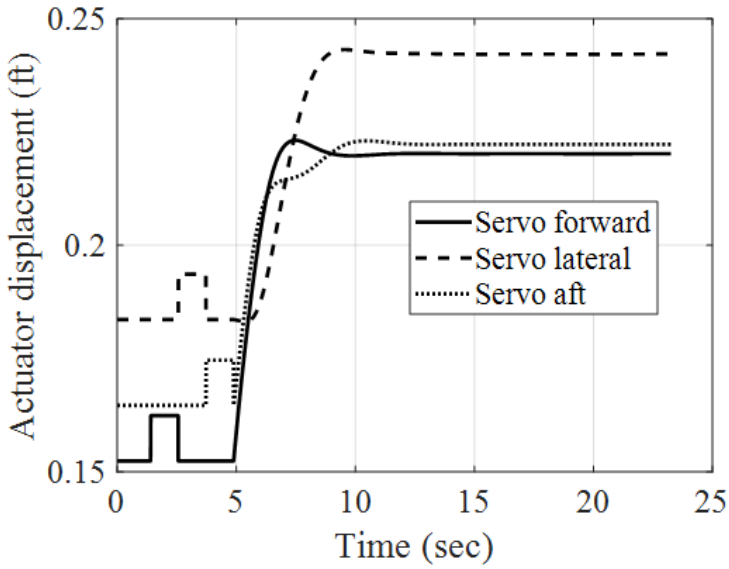

Fig. 2.5. Time history of the servo actuator input

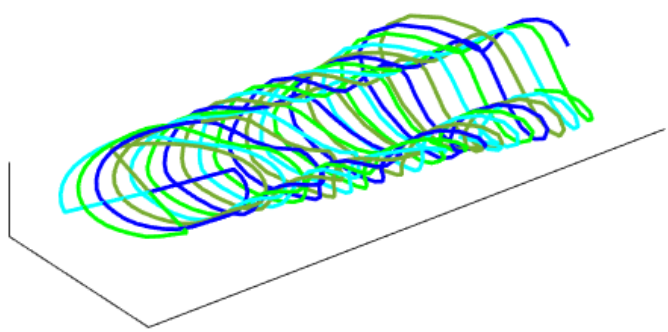

Fig. 2.6. Schematic of the free wake model

The trim analysis results are shown in Figs. 2.7 and 2.8. Although there is a discrepancy between the aerodynamic loads in the reference and the present result, such as the level of the mean lift, the oscillatory lift level is predicted similar to the reference. Since the flight condition C8513 corresponds to a descent maneuver, complex aerodynamic circumstances such as the blade-vortex interaction affects the rotor. As a consequence, it is expected that the discrepancy of the aerodynamic loads will be induced by the fidelity of the aerodynamic analysis included in DYMORE2. Also, one per revolution peak and the oscillatory load level of the structural loads are also predicted in a similar way as shown in the literatures. In conclusion, the fidelity of the representative rotor system is verified by the modal and trim analysis.

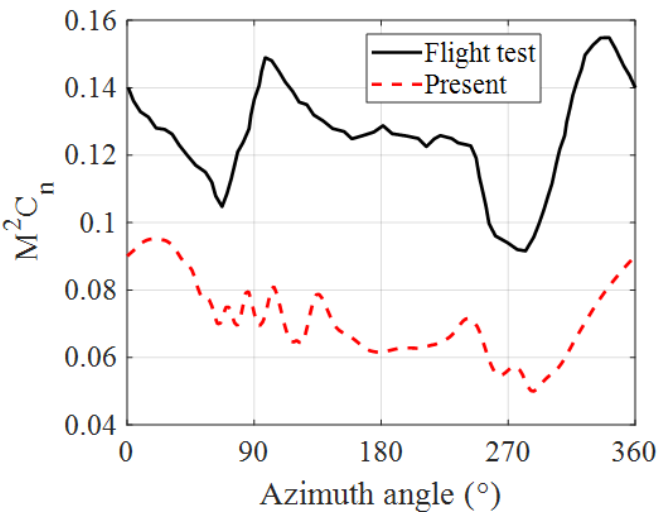

(a) Nondimensional normal force at 0.675R

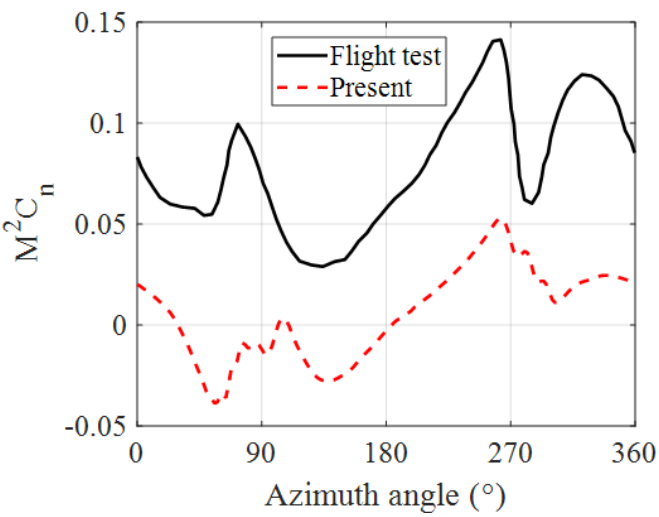

(a) Nondimensional normal force at 0.675R

Fig. 2.7. Sectional aerodynamic loads on the rotor blades

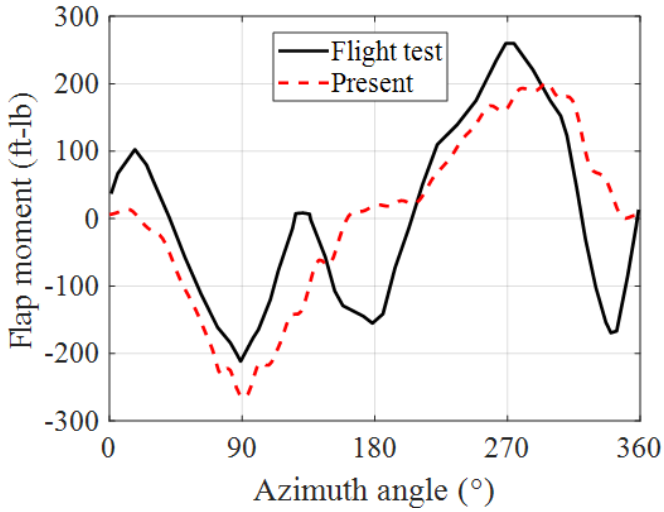

(a) Blade flapping moment at 0.3R

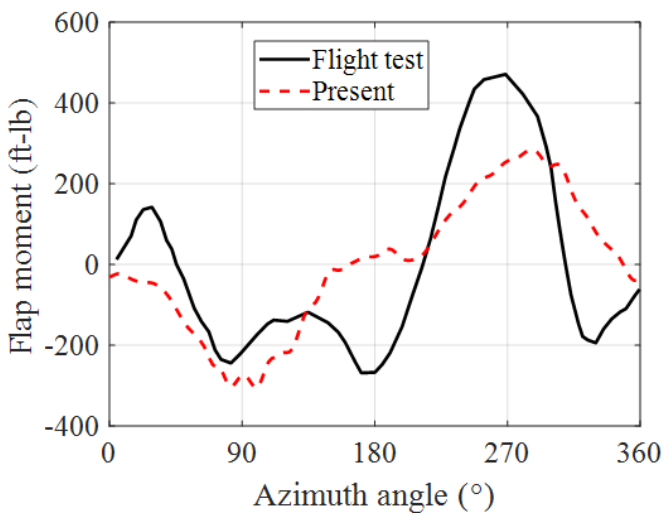

(b) Blade flapping moment at 0.5R

Fig. 2.8. Sectional structural loads of the rotor blades

Chapter 3

Higher Harmonic Control Simulation

In this chapter, the details will be described about the algorithm for the present higher harmonic control simulation. Since the controller input is the higher harmonic coefficient but the actual inputs consist of the motion of servo actuators, a derivation of the transformation from the servo actuator displacement to the higher harmonic coefficient will be given. By the present transformation matrix, the higher harmonic control simulation with an algorithm based on linear quadratic Gaussian (LQG) will be presented. Via the simulation, the vibration reduction capability of the LQG-based algorithm will be validated.

3.1 Conversion of the control input

To effectively reduce the vibration induced by unsteady external loads, it is important to design the analysis model appropriately. By the cancellation of the external loads from each blade, only the vibratory loads of N/rev frequency will be transferred to the shaft. In addition, the in-plane structural loads with N/rev frequency will be transformed into the N$\pm$1/rev frequencies due to the relationship of the rotating and non-rotating, or fixed frame. As a consequence, the dominative frequency components will be the N/rev and N$\pm$1/rev frequencies. To effectively control and reduce the vibratory loads, the control targets should be in the form of

harmonic vibratory loads at such frequencies.

The object quantity of the higher harmonic control is the vibratory loads in the main rotor shaft, and the control input is the linear displacements of the three servo actuators. Both the control targets and the control inputs are measured or determined with respect to the fixed frame. Figure 3.1 shows the block diagram of the present higher harmonic control algorithm. The controller matrix, K, receives the vibratory rotor hub loads signal and derives the output vector in the form of the higher harmonic coefficients. However, since the controller output is in the form of the higher harmonic coefficients, the transformation between the controller output and DYMORE2 input is required. The actual input of DYMORE2 is the displacements of the servo actuators. In order to accomplish such a transformation, the conversion block in Fig. 3. 1 act as the transformation matrix. The formulation of the conversion block is based on the relationship between the fixed frame swashplate actuator displacements and the orientation of the swashplate. The schematic of the servo actuators and the rotating swashplate is shown in Fig. 3. 2. In the schematic, each displacement of the servo actuators is denoted as u_0^L, u_0^F, and u_0^A. The swashplate can be modeled as a circular plate, and thus the collective input will be characterized by the displacement of the center of the circular plate. The displacement of the center will be denoted as Δz. Furthermore, the lateral and longitudinal cyclic controls are achieved by the rotation of the swashplate among the x- and y- axes. These rotation angles are defined as α_x and α_y for each direction.

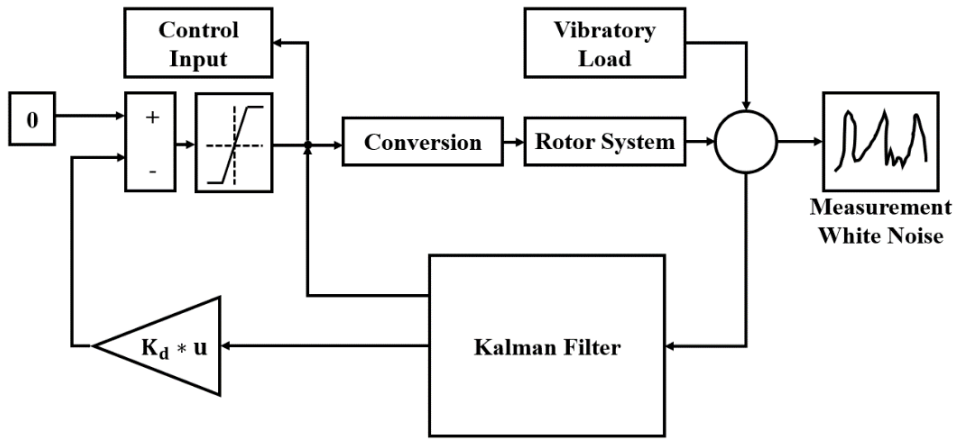

Fig. 3.1. Block diagram of the present LQG simulation

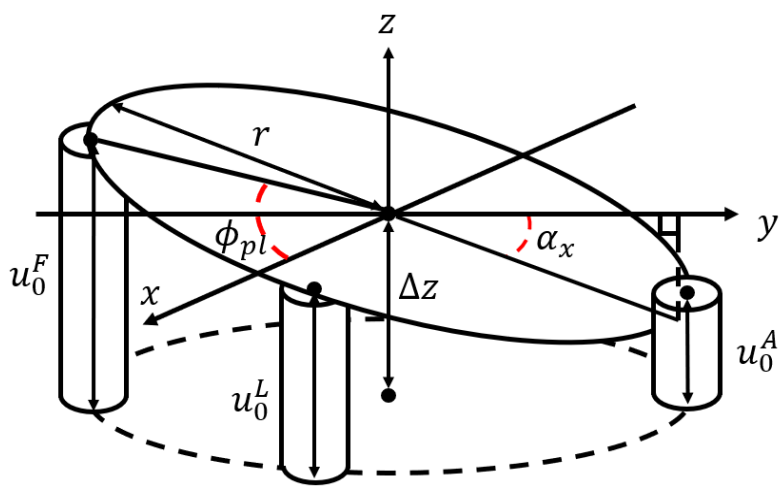

Fig. 3.2. Schematic of the rotating swashplate and the servo actuators

To derive the mathematical relationship between the displacements of the servo actuators and the higher harmonic coefficients, small angle displacement is assumed as Eq. (3.1).

$$\begin{Bmatrix} \boldsymbol{u_0^F} \\ \boldsymbol{u_0^L} \\ \boldsymbol{u_0^A} \end{Bmatrix} = \begin{bmatrix} \mathbf{1} & \boldsymbol{r\cos\phi_{pl}} & \boldsymbol{r\sin\phi_{pl}} \\ \mathbf{1} & \boldsymbol{-r\sin\phi_{pl}} & \boldsymbol{r\cos\phi_{pl}} \\ \mathbf{1} & \boldsymbol{-r\cos\phi_{pl}} & \boldsymbol{-r\sin\phi_{pl}} \end{bmatrix} \begin{Bmatrix} \boldsymbol{\Delta z} \\ \boldsymbol{\alpha_x} \\ \boldsymbol{\alpha_y} \end{Bmatrix} \tag{3.1}$$

By considering that the constant component of the control input, θ_0, may be expressed by the relationship $\Delta z = K_{cz}\theta_0$, and annotating variables in the fixed frame control input, Equation. (3.2) can be rewritten as follows.

$$\begin{Bmatrix} \boldsymbol{u_0^F} \\ \boldsymbol{u_0^L} \\ \boldsymbol{u_0^A} \end{Bmatrix} = \begin{bmatrix} \boldsymbol{K_{cz}} & \boldsymbol{r\cos\phi_{pl}} & \boldsymbol{r\sin\phi_{pl}} \\ \boldsymbol{K_{cz}} & \boldsymbol{-r\sin\phi_{pl}} & \boldsymbol{r\cos\phi_{pl}} \\ \boldsymbol{K_{cz}} & \boldsymbol{-r\cos\phi_{pl}} & \boldsymbol{-r\sin\phi_{pl}} \end{bmatrix} \begin{Bmatrix} \boldsymbol{\theta_0} \\ \boldsymbol{\theta_{1c}} \\ \boldsymbol{\theta_{1s}} \end{Bmatrix} \tag{3.2}$$

For the present rotor system, it is identified that $K_{cz} = 1.13$, and ϕ_{pl} is a constant that is equal to 31.2°. The i-th individual blade higher harmonic pitch input can be expressed as

$$\begin{aligned} \boldsymbol{\theta_{HHC}^i} = {} & \boldsymbol{\theta_c^N \cos N\psi + \theta_s^N \sin N\psi} \\ & \boldsymbol{+ \theta_c^{N+1} \cos\left\{(N+1)\psi + \frac{2\pi(i-1)}{N}\right\}} \\ & \boldsymbol{+ \theta_s^{N+1} \sin\left\{(N+1)\psi + \frac{2\pi(i-1)}{N}\right\}} \\ & \boldsymbol{+ \theta_c^{N-1} \cos\left\{(N-1)\psi - \frac{2\pi(i-1)}{N}\right\}} \\ & \boldsymbol{+ \theta_s^{N-1} \cos\left\{(N-1)\psi - \frac{2\pi(i-1)}{N}\right\}} \end{aligned} \tag{3.3}$$

where $\psi_1 = \psi$ is the azimuth angle of the first blade.

Applying the multi-blade coordinate transform to obtain the fixed frame HHC input, which consist of only N/rev frequency yields

$$\begin{aligned}
\boldsymbol{\theta_0} &= \boldsymbol{\theta_c^N \cos N\psi + \theta_s^N \sin N\psi} \\
\boldsymbol{\theta_{1c}} &= \boldsymbol{\left(\theta_c^{N+1} + \theta_c^{N-1}\right)\cos N\psi + \left(\theta_s^{N+1} + \theta_s^{N-1}\right)\sin N\psi} \\
\boldsymbol{\theta_{1s}} &= \boldsymbol{\left(\theta_s^{N+1} - \theta_s^{N-1}\right)\cos N\psi + \left(\theta_c^{N-1} - \theta_c^{N+1}\right)\sin N\psi} \\
\boldsymbol{\theta_2} &= \boldsymbol{0}
\end{aligned} \tag{3.4}$$

Substituting Eq. (3.4) in Eq. (3.2) gives a cosine and sine basis representation of the swashplate actuator HHC input.

$$\begin{bmatrix} \boldsymbol{u_{Nc}^F} \\ \boldsymbol{u_{Ns}^F} \\ \boldsymbol{u_{Nc}^L} \\ \boldsymbol{u_{Ns}^L} \\ \boldsymbol{u_{Nc}^A} \\ \boldsymbol{u_{Ns}^A} \end{bmatrix} = \begin{bmatrix} \boldsymbol{K_{cz}} & & \boldsymbol{r\cos\phi_{pl}} & & \boldsymbol{r\sin\phi_{pl}} & \\ & \boldsymbol{K_{cz}} & & \boldsymbol{r\cos\phi_{pl}} & & \boldsymbol{r\sin\phi_{pl}} \\ \boldsymbol{K_{cz}} & & \boldsymbol{-r\sin\phi_{pl}} & & \boldsymbol{r\cos\phi_{pl}} & \\ & \boldsymbol{K_{cz}} & & \boldsymbol{-r\sin\phi_{pl}} & & \boldsymbol{r\cos\phi_{pl}} \\ \boldsymbol{K_{cz}} & & \boldsymbol{-r\cos\phi_{pl}} & & \boldsymbol{-r\sin\phi_{pl}} & \\ & \boldsymbol{K_{cz}} & & \boldsymbol{-r\cos\phi_{pl}} & & \boldsymbol{-r\sin\phi_{pl}} \end{bmatrix} \tag{3.5}$$

$$\begin{bmatrix} \theta_c^N \\ \theta_s^N \\ \theta_c^{N+1} + \theta_c^{N-1} \\ \theta_s^{N+1} + \theta_s^{N-1} \\ \theta_s^{N+1} - \theta_s^{N-1} \\ \theta_c^{N-1} - \theta_c^{N+1} \end{bmatrix} = [M] \begin{bmatrix} 1 & & & & & \\ & 1 & & & & \\ & & 1 & & 1 & \\ & & & 1 & & 1 \\ & & & 1 & & -1 \\ & & -1 & & 1 & \end{bmatrix} \begin{bmatrix} \theta_c^N \\ \theta_s^N \\ \theta_c^{N+1} \\ \theta_s^{N+1} \\ \theta_c^{N-1} \\ \theta_s^{N-1} \end{bmatrix}$$

$$= \begin{bmatrix} K_{cz} & & r\cos\phi_{pl} & r\sin\phi_{pl} & r\cos\phi_{pl} & -r\sin\phi_{pl} \\ & K_{cz} & -r\sin\phi_{pl} & r\cos\phi_{pl} & r\sin\phi_{pl} & r\cos\phi_{pl} \\ K_{cz} & & -r\sin\phi_{pl} & r\cos\phi_{pl} & -r\sin\phi_{pl} & -r\cos\phi_{pl} \\ & K_{cz} & -r\cos\phi_{pl} & -r\sin\phi_{pl} & r\cos\phi_{pl} & -r\sin\phi_{pl} \\ K_{cz} & & -r\cos\phi_{pl} & -r\sin\phi_{pl} & -r\cos\phi_{pl} & r\sin\phi_{pl} \\ & K_{cz} & r\sin\phi_{pl} & -r\cos\phi_{pl} & -r\sin\phi_{pl} & -r\cos\phi_{pl} \end{bmatrix} \begin{bmatrix} \theta_c^N \\ \theta_s^N \\ \theta_c^{N+1} \\ \theta_s^{N+1} \\ \theta_c^{N-1} \\ \theta_s^{N-1} \end{bmatrix} \tag{3.6}$$

The transformation matrix in the last row in Eq. (3.6) is a full rank matrix, and which is invertible. It indicates a relationship between the swashplate HHC actuator input and the practical rotating frame blade HHC input.

$$\begin{aligned} F_{x,N} - F_{x0,N} &= \delta F_{xc}^N \cos N\psi + \delta F_{xs}^N \sin N\psi \\ F_{y,N} - F_{y0,N} &= \delta F_{yc}^N \cos N\psi + \delta F_{ys}^N \sin N\psi \\ F_{z,N} - F_{z0,N} &= \delta F_{zc}^N \cos N\psi + \delta F_{zs}^N \sin N\psi \\ M_{x,N} - M_{x0,N} &= \delta M_{xc}^N \cos N\psi + \delta M_{xs}^N \sin N\psi \\ M_{y,N} - M_{y0,N} &= \delta M_{yc}^N \cos N\psi + \delta M_{ys}^N \sin N\psi \\ M_{z,N} - M_{z0,N} &= \delta M_{zc}^N \cos N\psi + \delta M_{zs}^N \sin N\psi \end{aligned} \tag{3.7}$$

3.2 Algorithm for the higher harmonic control simulation

After the model for the control is determined, the algorithm for the vibration control also should be determined. In the early period of the higher harmonic control research, the popular algorithm for higher harmonic control was the T-matrix based algorithm. With the T-matrix based algorithm, it is assumed that the transfer function matrix is known so that the swashplate motion to reduce the vibratory loads can be obtained by an inverse matrix of the transfer function. However, as Hall pointed out

[16], the T-matrix assumes the relationship between the inputs and outputs as simple algebraic equations, it is only possible to evaluate its stability with Lyapunov function. However, still the relative stability of the T-matrix cannot be evaluated since the matrix consists of such simple algebraic equations. To clear such a problem, the algorithm for the present thesis modeled the system as a linear system, which can be denoted as Equation, (3.8)

$$\dot{\boldsymbol{x}} = \boldsymbol{A}\boldsymbol{x} + \boldsymbol{B}\boldsymbol{u} \tag{3.8}$$

The algorithm used in this thesis is proposed by the present authors and its details are included in [17]. To control the servo actuators, the linear time invariant (LTI) transfer function between the hub vibratory load and the higher harmonic control inputs will be established. Three hub load components are represented by the cosine and sine basis as in Eq. (3.7). A step input is given to the system, and then the perturbed output load in Eq. (3.7) is found by applying the recursive Fourier series filter to the output loads. The recursive Fourier series filter predicts and obtains harmonic Fourier coefficients of the signal at the k-th step.

To find the linear time invariant transfer function between the control input and output, a MATLAB function, “tfest” is used. By the function “tfest”, MATLAB will estimate the continuous-time transfer function in the state-space representation [18]. However, the state-space representation evaluated by the “tfest” function has 144 state variables of which number is too many to estimate the transfer function in a short time. A MATLAB function, “balred”, is used to reduce the number of the state variables. The function “balred” reduces the number of the state variables by the method based on the balanced singular perturbation approximation algorithm [19]. A comparison between the full-order and reduced matrix is shown in Fig. 3.3. In the most of frequency bands, the reduced matrix shows similar characteristics with that obtained by the full-order matrix.

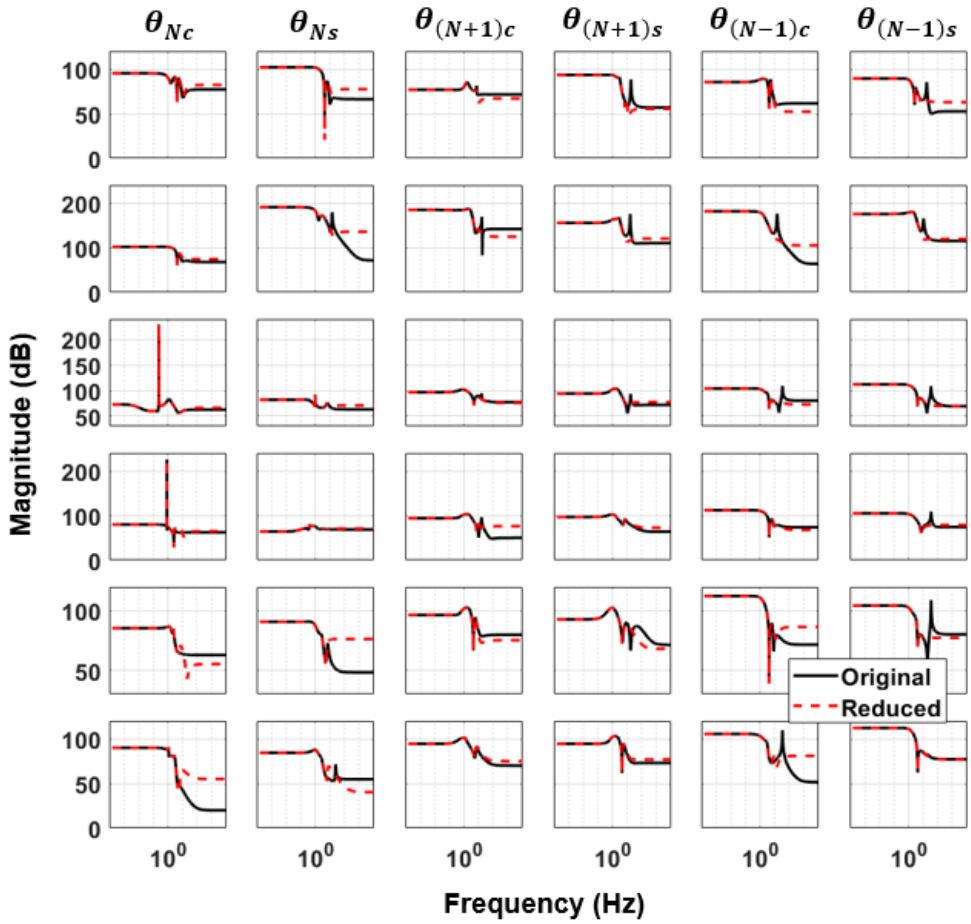

Fig. 3.3. Identified and reduced order system

To validate the full-order transfer function and the reduced matrices, simulation based on the unit load perturbation will be executed. Unit excitation of the target frequency component are imposed on DYMORE2 representation, the full-order linear time invariant, and the reduced linear time invariant transfer function matrix. The imposed excitation is the sine and cosine bases at N/rev and N$\pm$1/rev higher harmonic coefficients.

Although there exist a few discrepancies in the initial perturbation region, good agreement is achieved beyond an initial region. Since the perturbation is given in the manner of an open-loop actuation, it will be expected that when the control result is achieved from the reduced-order transfer function matrix, the result will be identical with that obtained by DYMORE2 computation.

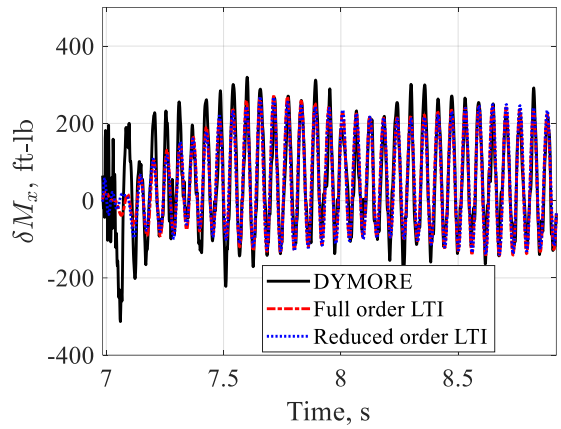

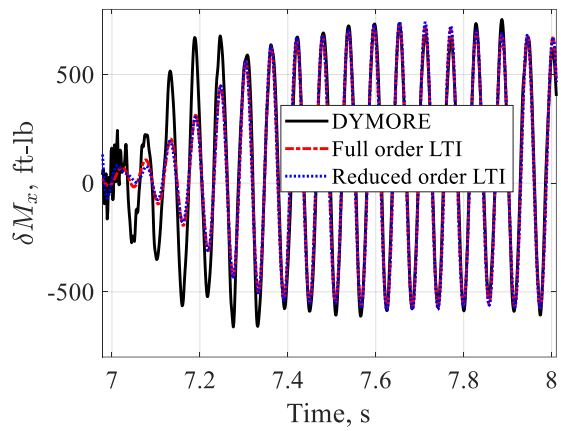

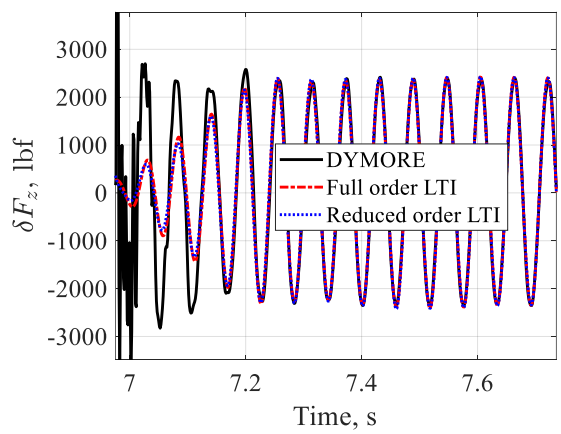

Fig. 3.4. Load perturbations for unit $\boldsymbol{\theta_c^N}$ input

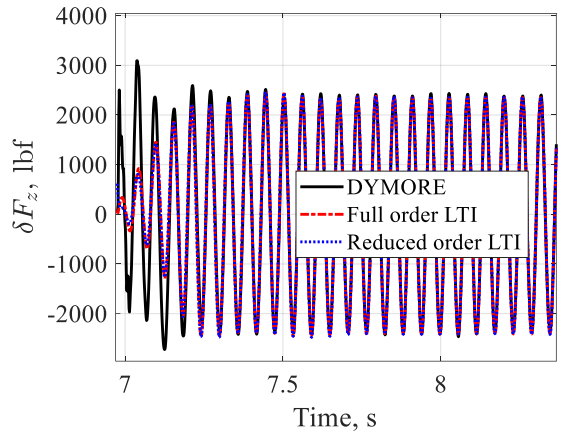

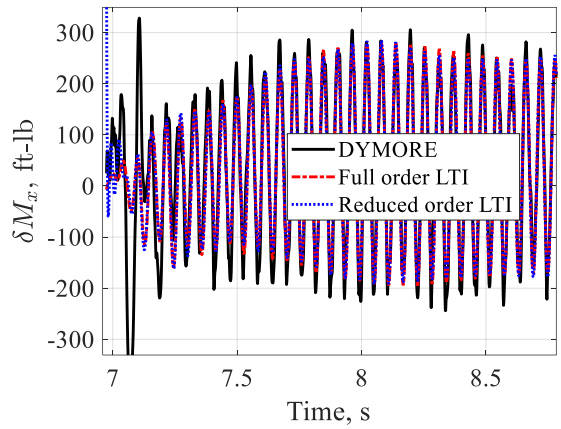

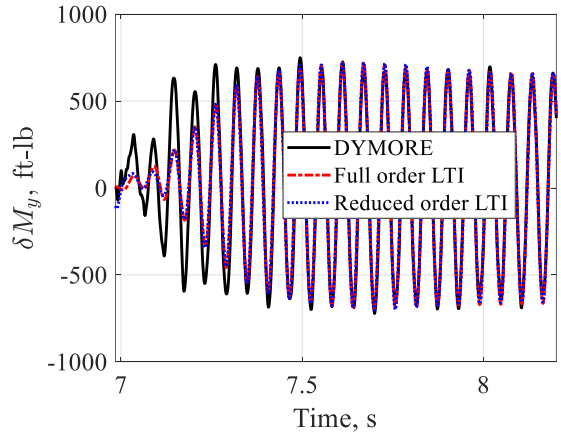

Fig. 3.5. Load perturbations for unit $\boldsymbol{\theta_s^N}$ input

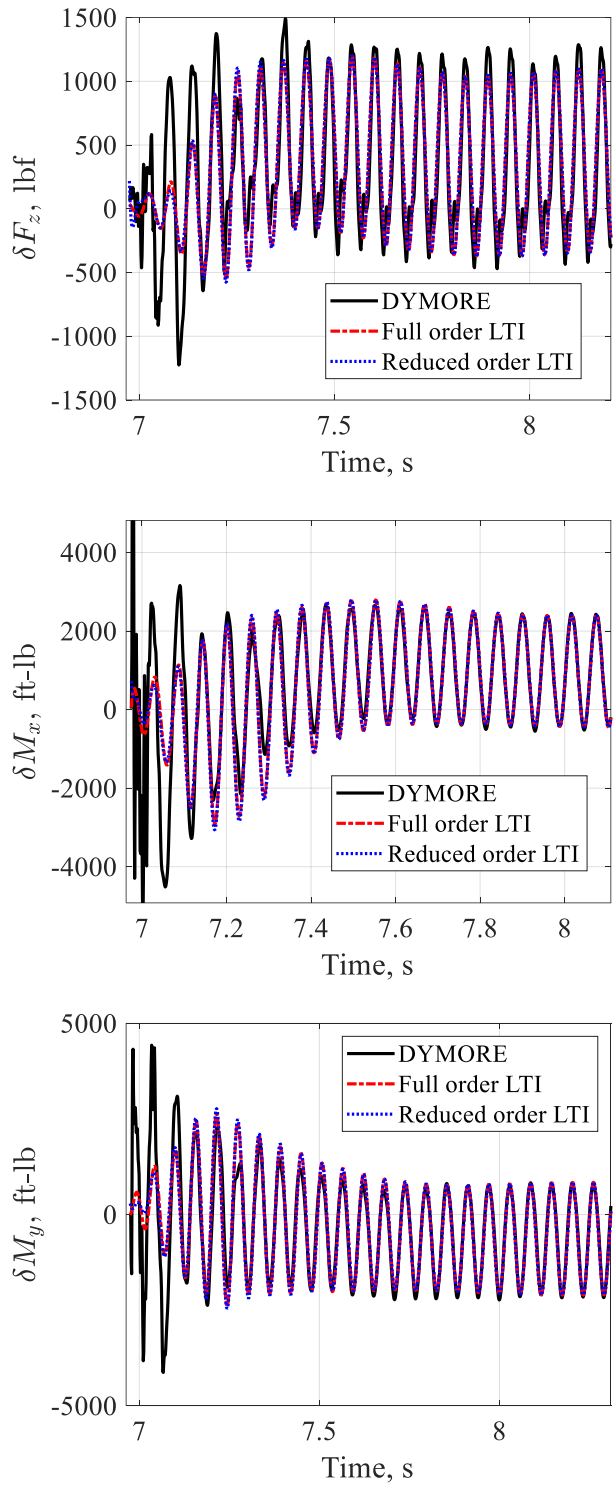

Fig. 3.6. Load perturbations for unit θ_c^{N+1} input

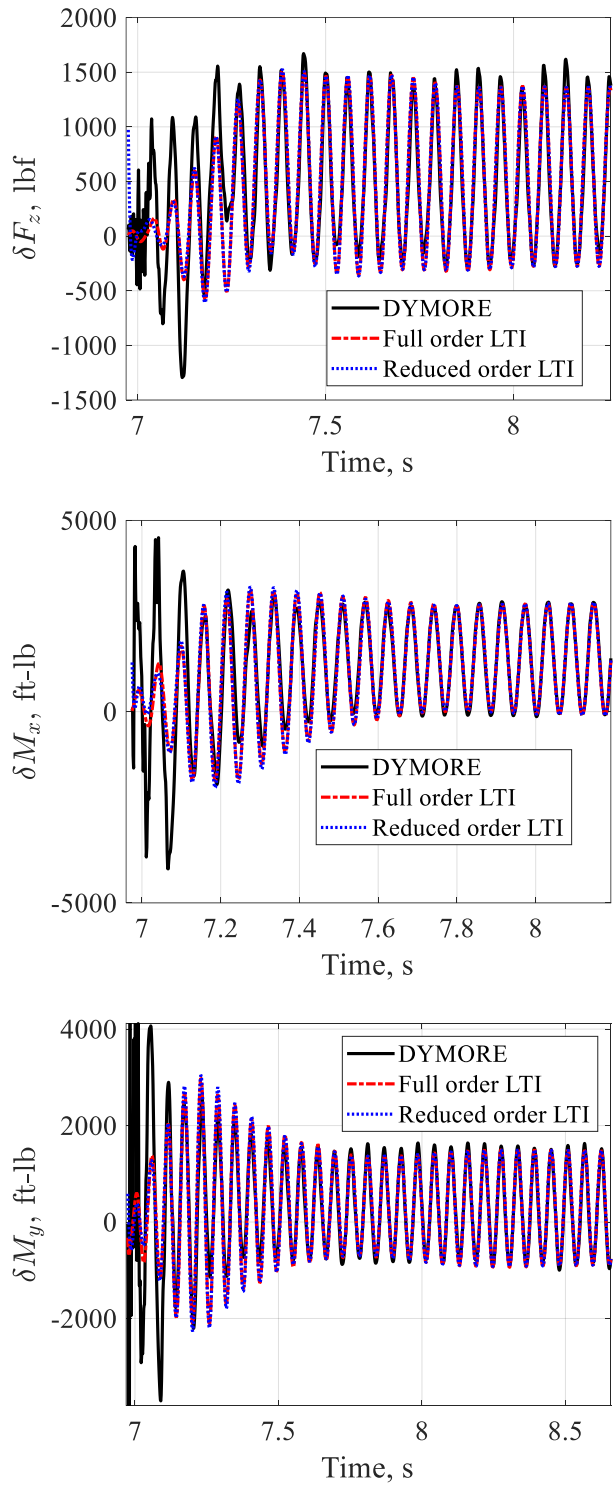

Fig. 3.7. Load perturbations for unit θ_s^{N+1} input

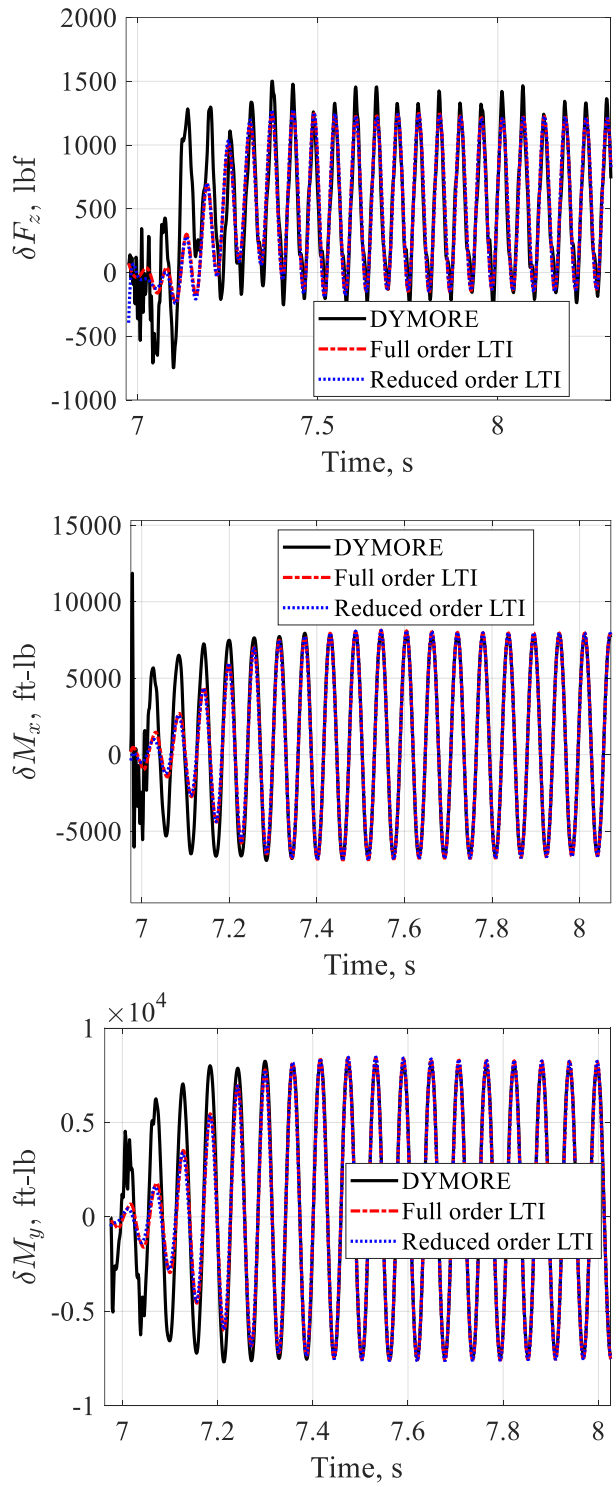

Fig. 3.8. Load perturbations for unit θ_c^{N-1} input

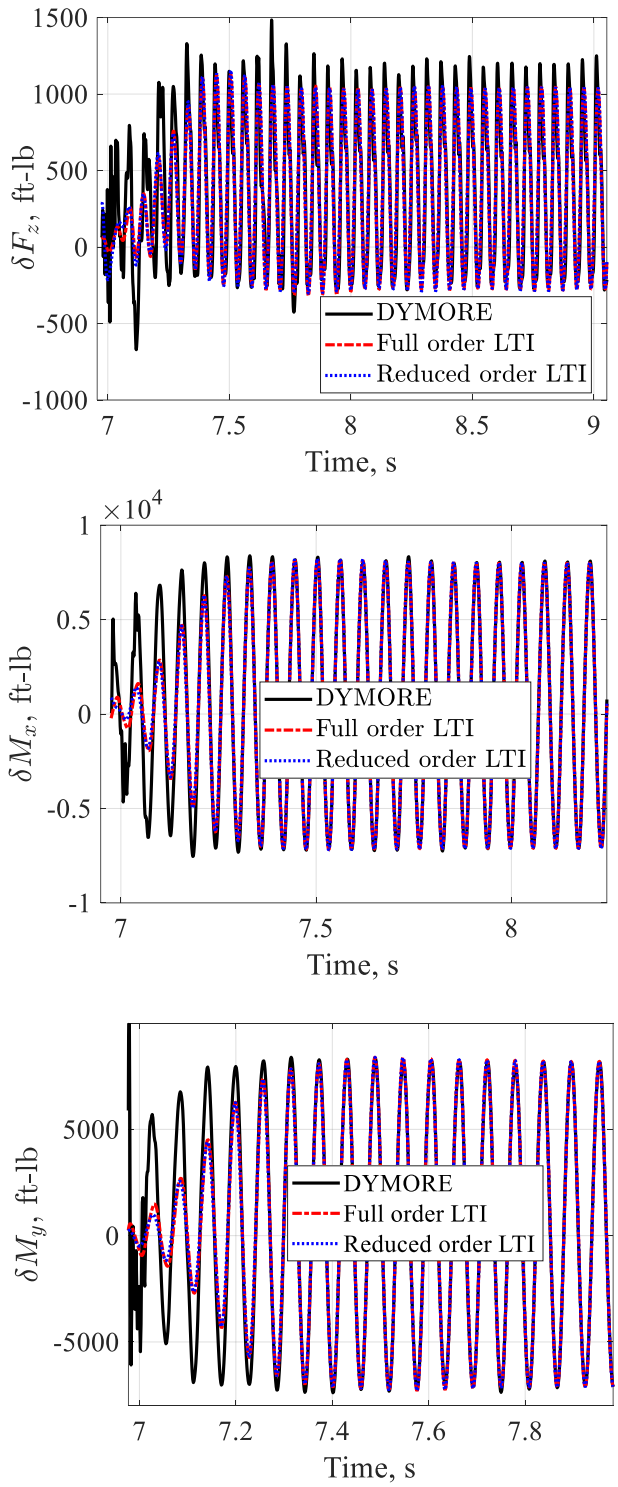

Fig. 3.9. Load perturbations for unit $\boldsymbol{\theta_s^{N-1}}$ input

After the transfer function matrix is configured, the controller will be created. By "tfest" and "balred" functions, the state variables of the system will be identified and reduced by the arithmetic relationship. As a consequence, it is not straightforward to recognize directly the physical meaning of the state variables. Also, under an experimental environment that the highly unsteady aerodynamic loads occur, stochastic sensor noise will affect to the measurement. To overcome such problem, Kalman filter will be used as an observer of the controller to estimate the state variable values.

The controller estimates a control input that minimize the cost function. The formulation of the cost function is given in Eq. (3.9).

$$\boldsymbol{J = \frac{1}{2}\int_0^\infty y^T Q y + u^T R u dt} \tag{3.9}$$

To minimize the cost function, the closed-loop system will be established with the weighting matrix Q and output weighting matrix R that are determined by the genetic algorithm optimization. The formulation of the input and output matrix are given in Eq. (3.10) and (3.11).

$$\boldsymbol{Q = \mathrm{diag}\{\frac{\alpha_1^2}{\{\max(F_{zc})\}^2}, \frac{\alpha_2^2}{\{\max(F_{zs})\}^2}, \frac{\alpha_3^2}{\{\max(M_{xc})\}^2}, \frac{\alpha_4^2}{\{\max(M_{xs})\}^2}, \frac{\alpha_5^2}{\{\max(M_{yc})\}^2}, \frac{\alpha_6^2}{\{\max(M_{ys})\}^2}\}} \tag{3.10}$$

(3.11)

$$\frac{\boldsymbol{\beta_4^2}}{\{\boldsymbol{max}(\boldsymbol{\theta_{4s}})\}^2}, \frac{\boldsymbol{\beta_5^2}}{\{\boldsymbol{max}(\boldsymbol{\theta_{5c}})\}^2}, \frac{\boldsymbol{\beta_6^2}}{\{\boldsymbol{max}(\boldsymbol{\theta_{5s}})\}^2}\}$$

As the importance of each control outputs can vary among themselves, penalty coefficients α_i and β_i to impose different weights on each component. After Q and R are selected, Then, MATLAB and the present analysis loop will be executed by the determined gain.

3.3 Numerical results

By the identified plant, the control authorities of the higher harmonic input are ascertained. Each of the load output is separated in three components, i.e., a constant and N/rev harmonic components at sine and cosine shapes. As N/rev or N±1/rev harmonic inputs are imposed on the plant, an unsteady perturbation will occur for certain initial duration. The plant will then become stable, and thus the constant component will be converged to zero value. Furthermore, the level of the sine and cosine bases will also become converged to the non-zero as certain stabilization duration is elapsed. Such non-zero level will be regarded as a control authority of the higher harmonic control input. For example, F_z component decomposition is shown in Fig. 3. 10.

In the similar manner, the identification of the control authority for the other structural load component is executed. For F_z, which may be interpreted as the shaft vertical load, it is identified that θ_c^N has the greatest control authority. On the other hand, for M_x and M_y, which may be interpreted as the shaft in-plane bending moment, N-1/rev and N+1/rev harmonic control inputs exhibit larger control authorities than that by N/rev harmonic control input. This suggets that the vertical load that is transmitted to the shaft will be at N/rev frequency in the fixed frame and the in-plane loads transmitted to the shaft be at the combination of N±1/rev frequencies [20].

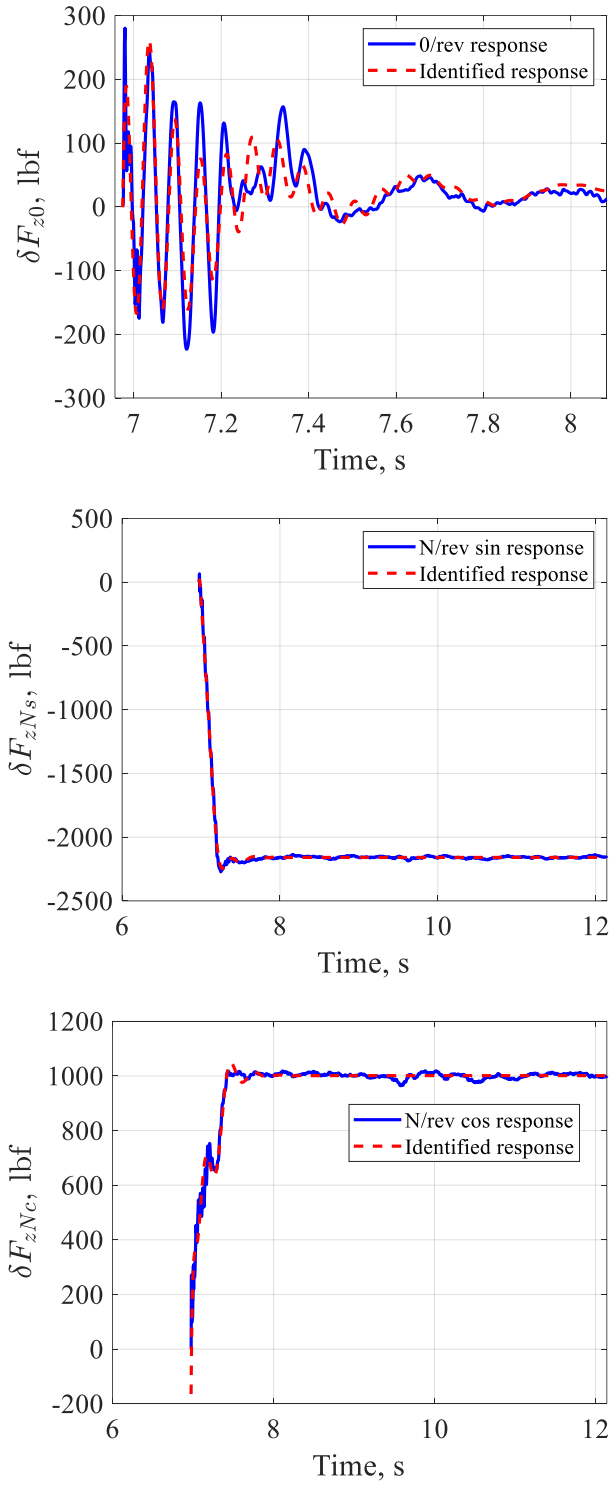

Fig. 3.10. Comparison of DYMORE and the identified plant

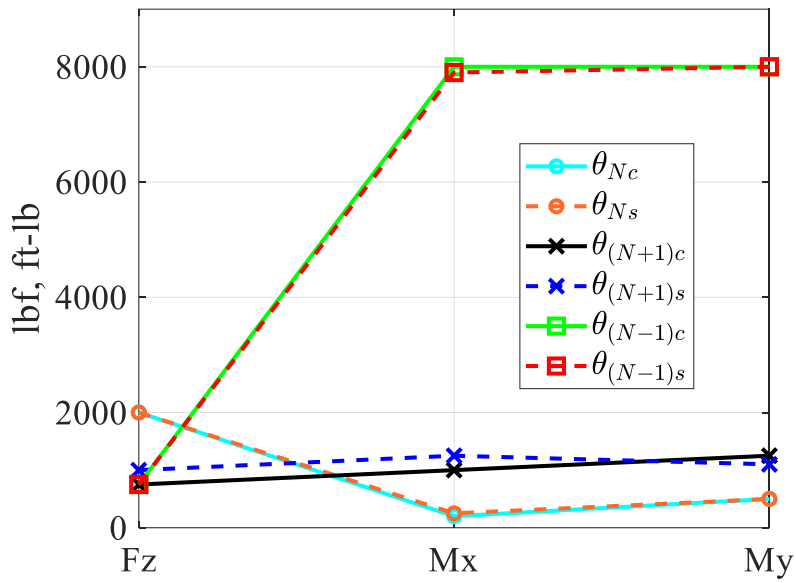

Fig. 3.11. Control authorities of the higher harmonic input

As an optimal gain is achieved via the reduced order representation, the higher harmonic control simulation by DYMORE2 computation and the reduced order one will be executed in the manner of an open-loop actuation. The comparison is shown in Fig. 3.12, along with the results by the dynamic analysis. The results are the structural load of the last revolution, and thus the horizontal axis quantity in the plot corresponds to the azimuth angle of the rotor blade. Also, the vertical axis quantity is the loads estimated in which the sensor is embedded. Since the rotor system consists of 4 blades, 4/rev frequency vibratory loads will be dominating. Such mechanism will be confirmed by the fact that the upper and lower peaks of the loads appear at a frequency of four occasions during each revolution.

The higher harmonic control gain achieved by the present algorithm is imposed on the plant, and the result in Fig. 3.12 shows that the present algorithm can effectively reduce the vibratory loads. Although the high frequency response is not captured with the reduced order representation, the vibration-reducing capability will be estimated. Furthermore, the level of the vibratory loads is plotted in Fig. 3.13. By adopting the present algorithm, 78% of the hub shear force, 74% of the hub rolling moment, and 43% of the hub pitching moment reduction are observed. In addition, the reduction capability estimated by DYMORE2 representation is larger than the estimation achieved by the reduced order representation.

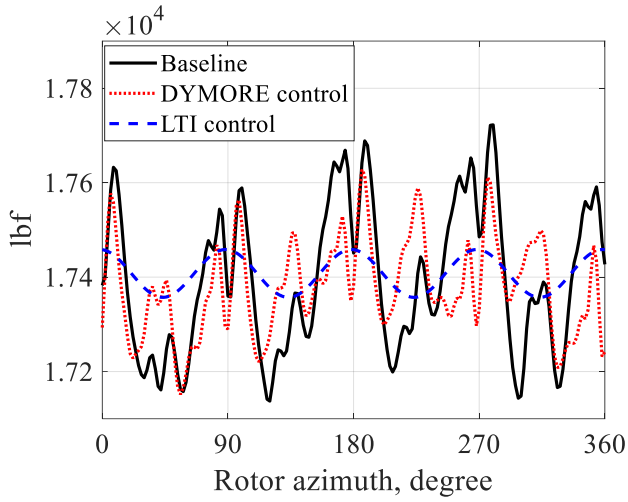

(a) Hub shear force prediction

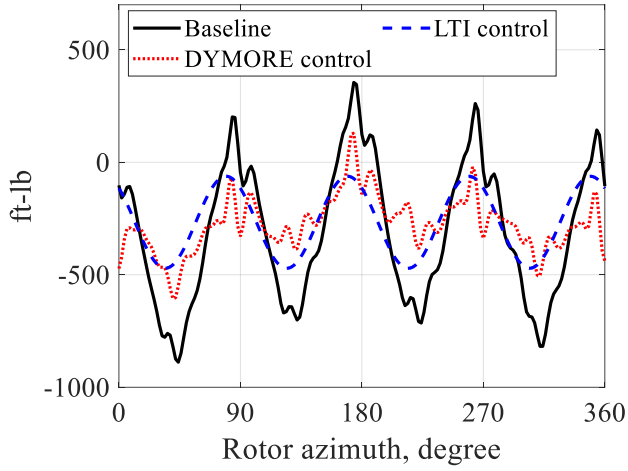

(b) Hub rolling moment prediction

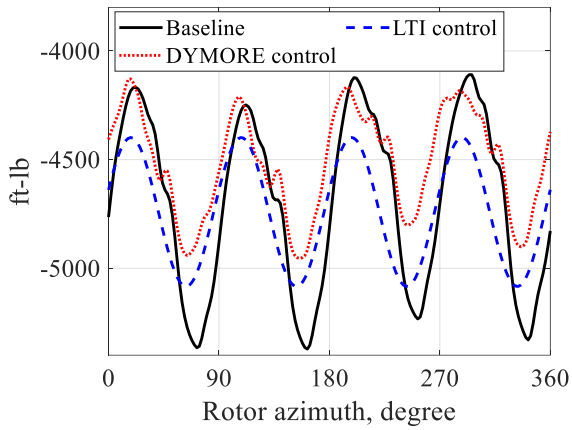

(c) Hub pitching moment preediction

Fig. 3.12. Vibration reduction capability prediction

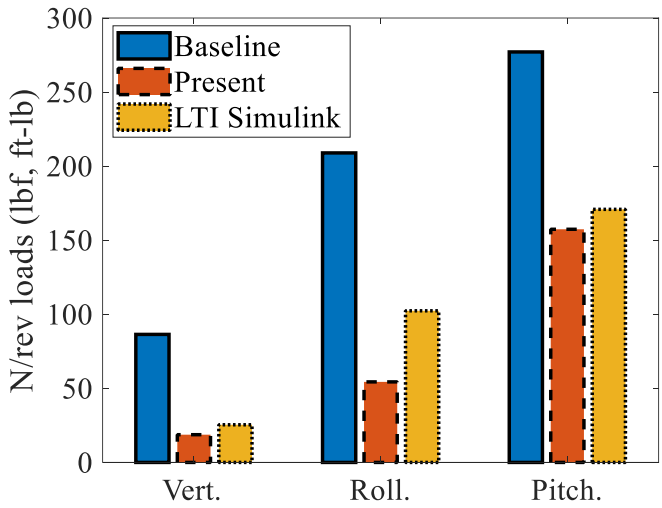

Fig. 3.13. N/rev vibratory load reduction

Chapter 4

Fuselage Attachment

In this chapter, the fuselage attachment will be discussed. To take account of the rotor-fuselage interaction, Herting's model order reduction method will be selected and implemented. Herting's method is one of the model order reduction methods, and its details will be explained in this chapter. Moreover, a simple example problem will be shown to verify the model order reduction capability of DYMORE2.

4.1 Validation of the model order reduction method

To reflect the structural response of the fuselage, the mode synthesis method will be introduced. The mode synthesis method is one of the model order reduction and sub-structuring techniques used in multibody dynamics analysis [21, 22]. Finite element model is characterized by the relevant matrices, i.e., stiffness, mass, and damping matrices. By combining the external load vector, the equation for transient analysis will be written as Eq. (4.1).

$$[\boldsymbol{M}]\{\ddot{\boldsymbol{x}}\} + [\boldsymbol{K}]\{\boldsymbol{x}\} = \{\boldsymbol{F}\} \tag{4.1}$$

If the target finite element representation uses fine grids and therefore the mass matrix $[M]$ and stiffness matrix $[K]$ become prohibitive size to analyze, it will take excessively much time and computational resources. To relieve such limitation,

the degree of freedom included in the representation will be reduced by using the modal coordinate. Each of the structural matrices can be divided into the boundary nodes of which degrees of freedom should be retained to the multi-body dynamics analysis and the interior nodes of which degrees of freedom can be reduced, as shown in Eq. (4.2).

$$[\boldsymbol{M}] = \begin{bmatrix} \boldsymbol{M_{BB}} & \boldsymbol{M_{BI}} \\ \boldsymbol{M_{IB}} & \boldsymbol{M_{II}} \end{bmatrix}, \qquad [\boldsymbol{K}] = \begin{bmatrix} \boldsymbol{K_{BB}} & \boldsymbol{K_{BI}} \\ \boldsymbol{K_{IB}} & \boldsymbol{K_{II}} \end{bmatrix} \tag{4.2}$$

In the Eq. (3.2), the subscript $(\cdot)_B$ stands for the boundary, and the subscript $(\cdot)_I$ stands for the interior. In the field of the mode synthesis approach, Craig-Bampton method was first suggested. The idea that divides the nodes into the boundary and interior nodes is identical, but Craig-Bampton method extracts the modes with the assumption of the fixed boundary condition. Since such assumption harms the accuracy of the transient analysis, Herting suggested the improved formulation with the assumption of free or unbound boundary condition [23]. For the present thesis, the structural matrices will then be reduced in its order by use of Herting's formulation.

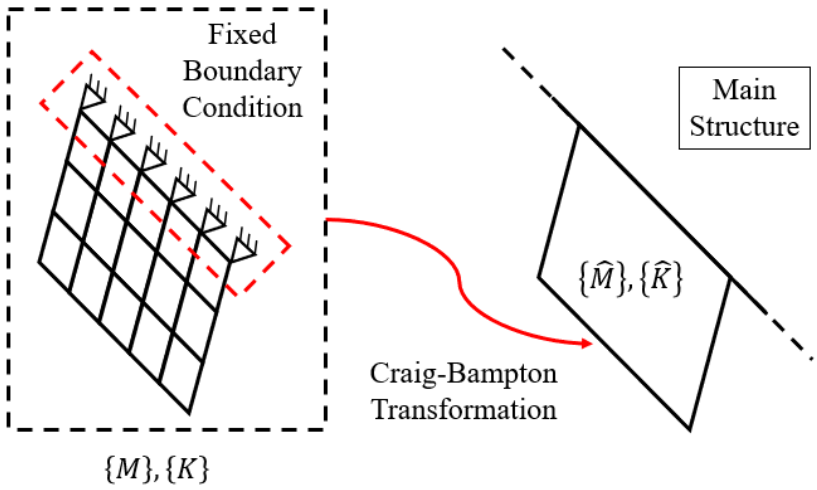

(a) Schematic for Craig-Bampton method

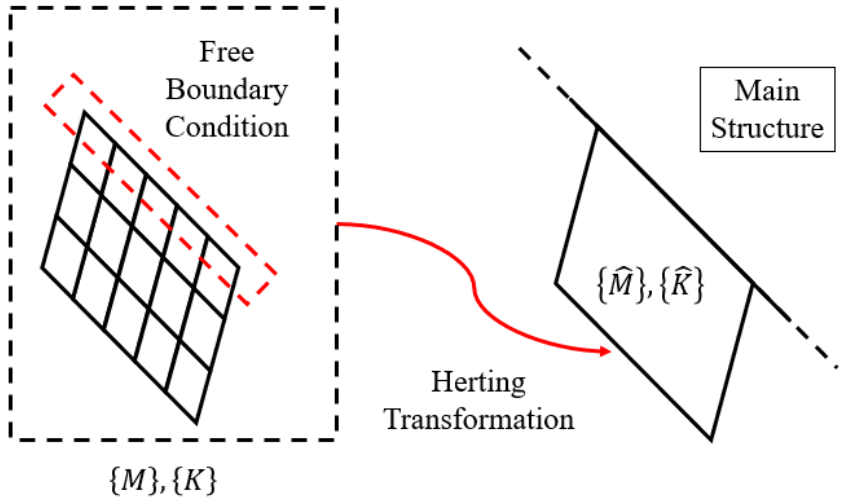

(b) Schematic for Herting-Transformation

Fig. 4.1. Schematic for model order reduction methods

By Herting's formulation, the substructures of which order will be reduced under the assumption that they have free interfaces so that no boundary constraints may be imposed. As a result, the eigenmodes will be divided into the rigid body modes and the elastic deformation modes as in Eq. (4.3).

$$\{\boldsymbol{\phi}\} = [\boldsymbol{\phi_R} \quad \boldsymbol{\phi_E}] \tag{4.3}$$

In Eq. (4.3), $\boldsymbol{\phi_R}$ is the rigid body mode vector and $\boldsymbol{\phi_E}$ is the elastic deformation vector. Again, each mode can be divided into a part corresponding to the boundary node and the other corresponding to the interior node. This division will be expressed as Equation (4.4).

$$\boldsymbol{\phi_R} = \begin{bmatrix} \boldsymbol{\phi_{BR}} \\ \boldsymbol{\phi_{IR}} \end{bmatrix}, \boldsymbol{\phi_E} = \begin{bmatrix} \boldsymbol{\phi_{BE}} \\ \boldsymbol{\phi_{IE}} \end{bmatrix} \tag{4.4}$$

By Herting's formulation, the transformation matrix can be configured as Equation (4.4)

$$\boldsymbol{H_H} = \begin{bmatrix} \boldsymbol{I} & \boldsymbol{0} & \boldsymbol{0} \\ \boldsymbol{G_{IB}} & \boldsymbol{H_{IR}} & \boldsymbol{H_{IE}} \end{bmatrix} \tag{4.5}$$

where

$$\boldsymbol{G_{IB}} = -(\boldsymbol{K_{II}})^{-1}\boldsymbol{K_{IB}} \tag{4.6}$$

$$\boldsymbol{H_{IR}} = -(\boldsymbol{K_{II}})^{-1}(\boldsymbol{M_{IB}} + \boldsymbol{M_{II}}\boldsymbol{G_{IB}})\boldsymbol{\phi_{BR}} \tag{4.7}$$

$$\boldsymbol{H_{IB}} = \boldsymbol{\phi_{IE}} - \boldsymbol{G_{IB}}\boldsymbol{\phi_{BE}} \tag{4.8}$$

Via Herting's transformation, the equation of motion is transformed from the coordinate of the boundary and interior nodes to the coordinate of the boundary nodes, the rigid body and elastic deformation modes. The equation for the mode coordinate will be expressed as Eq. (4.9).

$$[\hat{\boldsymbol{M}}]\{\ddot{\hat{\boldsymbol{x}}}\} + [\hat{\boldsymbol{K}}]\{\hat{\boldsymbol{x}}\} = \{\hat{\boldsymbol{F}}\} \tag{4.9}$$

where

$$\hat{\boldsymbol{M}} = \boldsymbol{H}_{\boldsymbol{H}}^{\boldsymbol{T}}\boldsymbol{M}\boldsymbol{H}_{\boldsymbol{H}}, \qquad \hat{\boldsymbol{K}} = \boldsymbol{H}_{\boldsymbol{H}}^{\boldsymbol{T}}\boldsymbol{M}\boldsymbol{H}_{\boldsymbol{H}}, \qquad \hat{\boldsymbol{F}} = \boldsymbol{H}_{\boldsymbol{H}}^{\boldsymbol{T}}\boldsymbol{F} \tag{4.10}$$

In DYMORE 2.0, Herting's model order reduction technique is implemented as the name of modal super element. To verify such modal super element function, a modal analysis and a simple transient analysis are attempted.

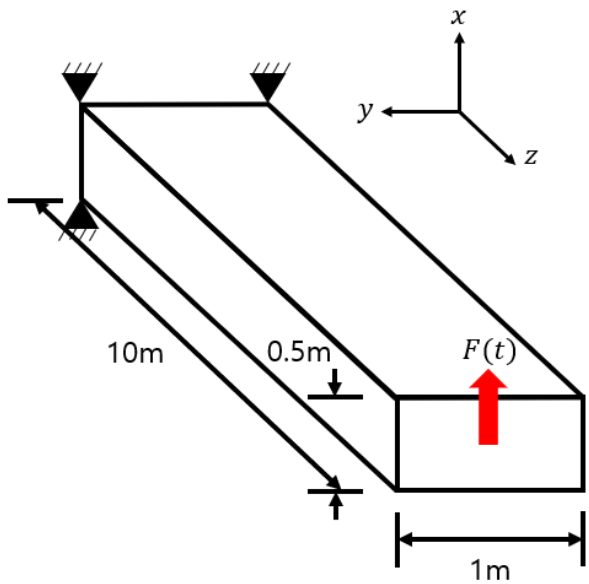

Fig. 4.2. Schematic of the rectangular hollow shell beam example

Table 4.1 Properties of the rectangular hollow shell

Characteristic	Metric
Width	1 m
Height	0.5 m
Length	10
Thickness	0.05m
Young's modulus	210 GPa
Density	7,850 kg/m3
Poisson's ratio	0.3

The schematic of the present analysis is shown in Fig. 4. 1. A step load in x-direction or a harmonic input is to be imposed on a rectangular hollow shell. The load is imposed on the center of the top face of the shell. Fixed boundary conditions are applied to the four corner nodes of the opposite face. The properties of the shell are summarized in Table 4.1. For the transient analysis, the following three loads are provided: (a) step load, (b) 4Hz harmonic load, and (c) 16Hz harmonic load. The scales of the loads are 10,000N. The reduced structural matrices for DYMORE2 modal super element inputs is extracted by ANSYS Mechanical APDL commands.

The validity of DYMORE2 modal super element is examined by comparison of ANSYS full-order model and ANSYS condensed part model. The ANSYS condensed part model is the model order reduction function of ANSYS, and the function uses the same method of DYMORE2. Modal analysis is executed, and the results are included in Table 2. First twelve eigenfrequencies are compared against the ANSYS results for the verification. Within first six eigenfrequencies of DYMROE2 and ANSYS modal analysis, highly accurate agreements are achieved. There are some discrepancies between the latter 6 eigenfrequencies, they still showed good agreements.

Transient analyses are then executed with three load conditions. The major parameter used for the comparison is the displacement of the node on which the force is imposed. The results of transient analysis are shown in Fig. 4. 2. Good agreement are also achieved for all three load conditions. The word CP in the legend of Fig. 4.2. stands for the condensed part.

Table 4.2 Eigenfrequencies of the rectangular hollow shell

ANSYS Full-order model (Hz)	ANSYS Condensed part (Hz)	DYMORE2 Modal super element (Hz)
4.9845	4.9845	4.9845
9.0814	9.0814	9.0814
31.424	31.424	31.424
54.166	54.166	54.166
57.091	57.093	57.093
81.817	81.819	81.819
110.52	111.09	111.09
120.436	120.46	120.46
136.88	136.92	136.92
138.07	138.13	138.13
138.75	138.75	138.75
164.98	165.06	165.06

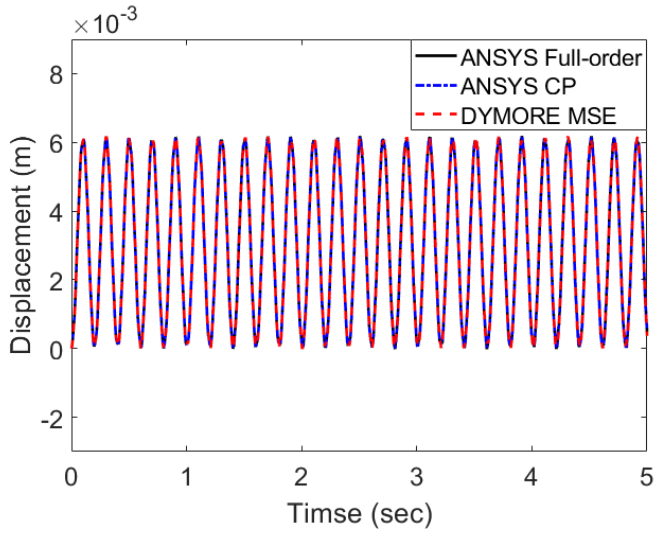

(a) Step load

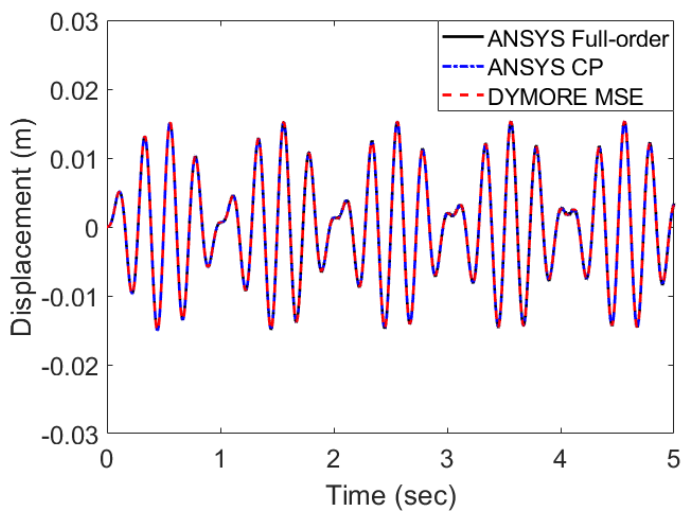

(b) 4Hz harmonic load

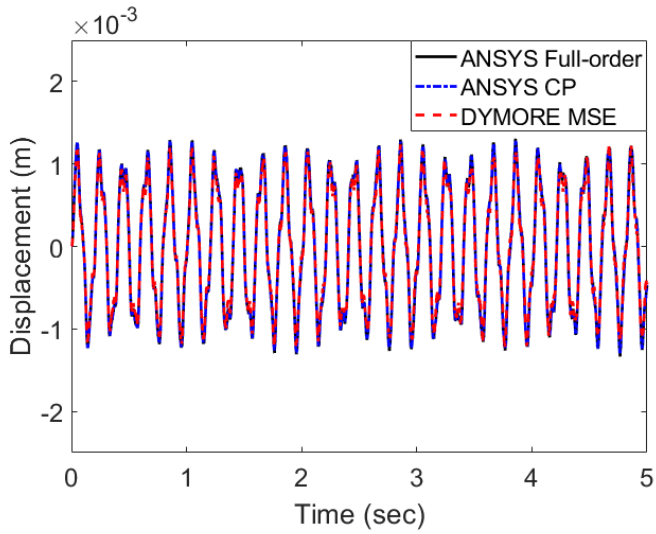

(c) 16Hz harmonic load

Fig. 4.3. Comparison of the nodal displacements

Chapter 5

Conclusion

In this thesis, the higher harmonic control simulation based on the physical approach is attempted. To validate the rotor modeling, the modal and trim analyses are executed. Next, the higher harmonic control simulation is executed. The algorithm for the simulation is based on LQG control algorithm. Finally, the vibration reducing capability is demonstrated.

5.1 Conclusion

For the verification of the representative rotor system, modal and trim analyses are executed. As a result of the modal analysis, comparison with the results included in the existing literatures is presented. Satisfactory agreement between the result of the present rotor representation and literatures is observed. The stiffness coefficient of the pitch link affects the higher eigenfrequencies, such as 3rd flap, 2nd lag, and 1st torsional frequencies. Since the comparison is executed against the other existing results, the stiffness coefficient is selected as the value that forces the higher mode eigenfrequencies to match closely with those in the other prediction. After the coefficient is determined, trim analysis is examined. The trim analysis is executed by using DYMORE2, a multibody dynamics analysis software. The flight condition is a descent maneuver. Although there is a discrepancy between the results of the

present analysis and the other existing ones, good agreement is achieved upon the mean lift, 1/rev peak and the oscillatory load.

Finally, the higher harmonic control simulation is examined. To avoid the disadvantage of T-matrix algorithm, which has been used mostly as a higher harmonic control, the algorithm for the present simulation is based on LQG algorithm. The controller input is N/rev structural load transmitted to the shaft, and the output is the higher harmonic coefficients at N/rev and N$\pm$1/rev frequencies. Since DYMORE2 control input is in the form of the displacement of the servo actuators, the relationship between the higher harmonic coefficients and the servo actuator displacements is derived. The linear time invariant representation is obtained by the relationship derived by a MATLAB function, “tfest.” Then for the speed-up of the search of the optimal gain, the number of the state variables is reduced by a MATLAB function, “balred”. The identified full-order system and reduced system are verified by the comparison on N/rev structural load response. Finally, the higher harmonic control simulation is examined in a manner of open-loop actuation. An optimal control input in the form of the higher harmonic coefficient is achieved by the linear time invariant representation, and imposed on the one built by DYMORE2. As a result, the hub shear force is reduced by 78%, as well as the hub rolling moment by 73.9% and the hub pitching moment by 43%.

To take account the rotor-fuselage interaction, Herting’s model order reduction approach is adopted. By applying Herting’s method, the nodal coordinate is transformed into the modal coordinate so that the number of the degrees of freedom

may be reduced. To verify the model order reduction capability of DYMORE2, an example problem of a simple shell is analyzed. Modal and transient dynamic analysis is achieved. For the transient analysis, the nodal tip load is imposed on a cantilevered rectangular hollow beam. As a result of comparison, good agreement between the results of the modal and transient analysis is achieved.

5.2 Recommendation for the future work

The followings are suggested for the future tasks to approve the fidelity of the control simulation.

1. The coupling of computational structural dynamics (CSD) and computational fluid dynamics (CFD) will be introduced. If rotorcraft is in a descent maneuver condition, blade vortex interaction will make such non-linear aerodynamic loads. Also, when the rotorcraft is in a high-speed forward flight, compressibility effect will appear at the tip of the blade so that a shock may be developed at the region. To catch the corresponding complex aerodynamic phenomena, high-fidelity CFD will be recommended.
2. To precisely realize the dynamic response of the fuselage, an improved configuration of the fuselage will be attached. The semi-monocoque structure of the fuselage will be idealized by an internal support, such as a stringer and frame.
3. To find an optimal control input considering the unsteady plant, closed-loop controller will be incorporated to DYMORE2. Based on LQG algorithm, Kalman filter will be selected as an observer since it is required to eliminate the noise or disturbances of the sensor input to adapt the experimental environment. To verify the vibration reduction capability of the present algorithm and the rotorcraft representation, an experiment will be executed. The sensor will be exposed to the highly unsteady aerodynamic loads so that the effect of the stochastic noise may be suppressed by Kalman filter.

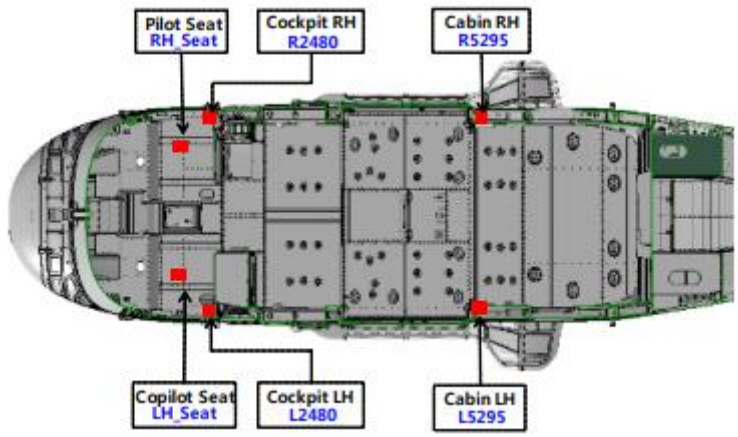

Fig. 5.1. Positions of the vibration level measurement for flight test [24]

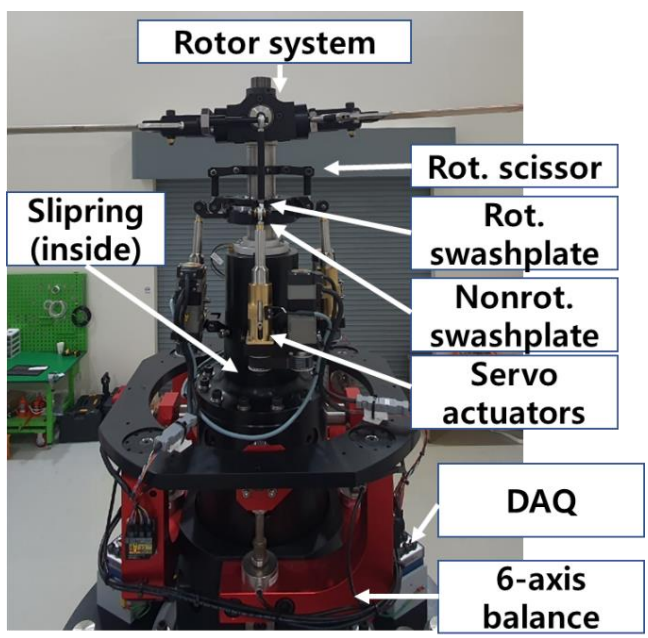

Fig. 5.2. SNUF experiment instrument configuration [25]

References

[1] Reichert, G., "Helicopter vibration control – a survey", *Vertica*, Vol. 5, (1), 1980, pp. 1-20.

[2] Johnson, W., *Helicopter Theory*, Princeton University Press. Princeton, NJ, 1980, pp. 808-813.

[3] Friedman, P. P., "On-blade control of rotor vibration, noise, and performance: Just around the corner? The 33rd Alexander Nikolsky Honorary Lecture," *Journal of the American Helicopter Society*, Vol. 5, (4), pp. 1-37.

[4] Taylor, R., B., Zwicke, P. E., Gold, P., and Miao, W., "Analytical design and evaluation of an active control system for helicopter vibration reduction and gust response alleviation," NASA-CR-152377, 1980.

[5] Oleary, J. J., Kottapalli, S. B. R., and Davis, M. W., "Adaptation of a modern medium helicopter (Sikorsky S-76) to higher harmonic control," *NASA Ames Research Center Rotor Dynamics 1984*, 1985.

[6] Johnson, W., *Self-tuning regulators for multicyclic control of helicopter vibration*, No. A-8719, 1982.

[7] Patt, D., Liu, L., Chandrasekar, K., Bernstein, D. S., and Friedmann P. P., "Higher-harmonic-control algorithm for helicopter vibration reduction revisited," *Journal of Guidance, Control, and Dynamics*, Vol. 28, (5), 2005, pp. 918-930.

[8] Hall, S. R., and Wereley, N. M., “Performance of higher harmonic control algorithms for helicopter vibration reduction,” *Journal of Guidance, Control, and Dynamics,* Vol. 16, (4), 1993, pp. 793-797.

[9] William, R., Tobias, P., and Manfred, H., “UH-60A Rotor and Coupled Rotor-Fuselage Simulation Framework Validation and Analysism” 45th European Rotorcraft Forum, Warsaw, September 2019.

[10] Howlett, J. J., “UH-60A Black Hawk Engineering Simulation Program. Volume 1: Mathematical model,” No. SER-70452, 1981.

[11] Bhagwat, M. J., and Leishman, J. G., “Generalized viscous vortex model for application to free-vortex and aeroacoustic calculations,” *Annual forum proceedings-American helicopter society*, Vol. 58, (2), American Helicopter Society, Inc, 2002.

[12] Ormiston, R. A., “An investigation of the mechanical airloads problem for evaluating rotor blade structural dynamics analysis,” American Helicopter Society 4th Decennial Specialists’ Conference on Aeromechanics, 2004.

[13] Bowen-Davies, G. M., Performance and loads of variable tip speed rotorcraft at high advance ratios, Ph.D Thesis, University of Maryland, College Park, 2015.

[14] Yeo, H., and Potsdam, M., “Rotor Structural Loads Analysis Using Coupled Computational Fluid Dynamics/Computational Structural Dynamics,” Journal of Aircraft, Vol. 53, (1), pp. 87-105.

[15] Sitaraman, J., and Roget, B., “Prediction of maneuver loads using a fluid-structure analysis,” Journal of Aircraft, Vol. 46, (5), pp. 1770-1784.

[16] Hall, S. R., and Werely, N. M., 1989, "Linear Control Issues in the Higher Harmonic Control of Helicopter Vibrations," *American Helicopter Society 45th Annual Forum Proceedings*, Boston, MA, May 22, pp. 955–972

[17] Im, B., Lee, C., Kee, Y., and Shin, S., "Investigation of linear higher harmonic control algorithm for rotorcraft vibration reduction," *Journal of Dynamic Systems, Measurement, and Control*, Vol. 143, (1), p.011008.

[18] Young, P. C., and Jakeman, A. J., 1980, "Refined Instrumental Variable Methods of Time-Series Analysis—Part III: Extensions," *International Journal of Control,* Vo.31, (4), pp. 741-768

[19] Varga, A., 1991, "Balancing-Free Square-Root Algorithm for Computing Singular Perturbation Approximations," Proceedings of the 30th Conference on Decision and Control, Brighton, UK, Dec. 11–13, pp. 1062–1065

[20] Alfred, G., and Garry, C. M., *Aerodynamics of the Helicopter*, Fredrick Ungar Publishing company, 1952, pp. 307-319.

[21] Nelson, K. J., and She, J. "Propeller Whirl Flutter Study using Multibody Dynamics Analysis with Component Mode Synthesis Element," AIAA SCITECH 2022 Forum, 2022, p. 1125.

[22] Bachau, O. A., Rodriguez, J., and Chen, S. Y., "Coupled rotor-fuselage analysis with finite motions using component mode synthesis," *Journal of the American Helicopter Society*, Vol. 49, (2), pp. 201-211.

[23] Herting, D. N., "A General Purpose, Multi-Stage, Component Modal Synthesis Method," Finite Element in Analysis and Design, Vol. 1, 1985, pp. 153-164.

[24] Kim, S. H., Lee, G. M., Shin, B. C., and Byun, J. H., “A Case Study of Vibration Reduction of Helicopter Development Configuration Using Graphic Analysis and Desirability Function,” *Journal of the Korean Society for Quality Management,* Vol. 43, (3), pp. 341-358.

[25] Im, B., Ryi, J., Rhee, W., Lee, H., Kong, K., and Claire, D, P., “Open-Loop Hover Experiment of a Mach-Scaled SNUF Rotor for Active Vibration Control,” 48th European Rotorcraft Forum, Winterthur, September 2022

국문초록

물리적 접근법에 기반한 LQG 알고리즘 고조화 제어 시뮬레이션

공건혁

서울대학교 대학원

항공우주공학과

회전익기는 비행 시 심각한 수준의 비정상 공기력에 노출되며, 이에 따라 높은 수준의 진동과 소음이 유발된다. 그러한 문제를 해결하기 위하여, 복수의 진동 및 소음 제어 방법론이 시도되어 왔다. 아이솔레이터와 흡진기 등으로 대표되는 수동적 방법론이 지속적으로 연구되었으나, 미 NASA 에서 제시한 진동 수준을 만족하는 제어 성능은 달성 불가하였다. 이에 따라 능동적 진동 제어 방법론이 연구되어 왔다. 고조화 제어 방법론은 능동적 진동 제어 방법론의 하나로, 가장 성숙되었으며 보장된 방법론으로 평가받았다. 이러한 고조화 제어 방법론에 관하여 시뮬레이션을 통한 연구 자료가 다수 존재하나, 로터 시스템의 물리적 구조가 고려된 연구는 소수에 불과하였다.

본 논문에서는 물리적 접근법에 기반한 고조화 제어 시뮬레이션이

수행되었다. 시뮬레이션의 구성은 UH-60A Black Hawk 기종의 물리적 구조를 기반으로 작성되었다. 로터 시스템은 블레이드, 댐퍼, 피치 링크, 힌지, 시저, 서보 작동기와 샤프트로 구성되었다. 각 블레이드의 피치 각은 비회전 스와시플레이트에 부착된 서보 작동기의 운동을 통해 조절된다. 로터 시스템의 실제 모델 충실도는 모드 해석과 트림 해석 결과의 비교를 통해 검증되었다.

다음 장에서, 본 논문의 시뮬레이션에 사용된 고조화 제어 알고리즘이 소개된다. 선형 제곱 가우시안에 기반하여, 진동 제어를 위한 최적 제어 값을 습득한다. 시스템 식별과 변수 축소는 MATLAB 함수를 통해 이루어졌다. 고조화 제어 시뮬레이션은 다물체 동역학 해석 소프트웨어 DYMORE 를 통해 이루어졌으며, 최대 78%의 진동 하중 감소에 달하는 진동 감소 성능을 확인하였다.

최종장에서, 동체의 반응 모사가 시연된다. 동체의 동적 응답을 반영하기 위해 Herting 의 차수 축소 기법이 도입되었다. Herting 기법을 통해, 세부 구조물의 자유도는 절점 단위에서 모드 단위로 축소된다. DYMORE 의 차수 축소 기능을 검증하기 위해, 사각형의 내부가 빈 보 구조물 예제에 대해 모드 해석과 시간 과도 동적 응답 해석이 진행되었다. 또한 동체 구조물을 모사하기 위한 구조물의 세부적인 사항이 제시되었다.

주제어: 고조화 제어, 능동 진동 제어, 요소 모드 합성법

학번: 2021-20832